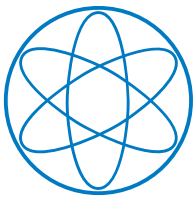

Technical University of Munich
Physics Department

Max Planck Institute
for Physics

Master's Thesis

Systematic Uncertainties of the KATRIN Neutrino Mass Measurement Associated with Beta Decays on the Rear Wall of the Experiment

Systematische Unsicherheit der Neutrinomassenbestimmung von KATRIN im Zusammenhang mit Betazerfällen auf der Rückwand des Experiments

Author:	Matthias Weidenthaler
Supervisor:	Prof. Dr. Susanne Mertens
Second Reviewer:	Prof. Dr. Bastian Märkisch

March 12th, 2022

Declaration of Authorship

German:

Ich versichere hiermit, dass ich die vorliegende Masterarbeit im Masterstudiengang Kern-, Teilchen- und Astrophysik selbstständig verfasst, und nur die angegebenen Hilfsmittel und Materialien verwendet habe.

English:

I hereby declare, that I have written this Master's thesis as part of the Nuclear, Particle and Astrophysics master program independently and that I have only used the acknowledged external resources.

Matthias Weidenthaler

Munich, February 11th 2022

Abstract

The existence of neutrinos and their properties have wide-ranging implications for particle physics and cosmology. Neutrino oscillation experiments prove that at least two neutrino mass eigenstates are non-zero and provide lower limits. Yet according to present knowledge the value of the absolute mass scale still remains undetermined. The KArlsruhe TRItium Neutrino experiment (KATRIN) is designed to measure the value of the effective electron neutrino mass with a sensitivity of $200\,\mathrm{meV/c^2}$ (90 % CL).

For that beta decays of gaseous tritium are observed. Since tritium circulation started, parts of the KATRIN experimental setup (in particular the *rear wall*) are unintentionally gradually being radioactively contaminated by charged and neutral particles from the tritium source. Beta decays stemming from this contamination comprise a time-dependent non-uniform background at the $< 1\,\%$ level in neutrino mass measurements.

As the detailed shape of this spectrum is unknown, the goal of this thesis was to find a suitable description of the rear wall spectrum for correcting the corresponding background in KATRIN neutrino mass campaigns from June 2020 to June 2021. Low statistics data from multiple dedicated rear wall characterization measurements was used to develop empirical and partly empirical models based on features of typical beta decay spectra and to evaluate their impact on the central value and the uncertainty of the KATRIN neutrino mass result.

The rear wall spectrum was found to cause a significant bias of the neutrino mass result which could be corrected. The additional systematic uncertainty was estimated to be smaller than $0.01\,\mathrm{eV^2}$ on the squared neutrino mass in the current energy range setting.

These results form the basis of further analyses for future data releases.

Contents

Chapter 1

Neutrino Physics

1.1 Neutrino Discovery

The idea of a new non-charged particle, later called neutrino, was first proposed by Wolfgang Pauli in 1930[1] to explain the continuous energy spectrum of electrons emitted in beta decays. A first experimental confirmation of this idea was achieved by Cowan and Reines in 1956[2] observing nuclear reactor neutrinos through inverse beta decay reactions

$$\bar{\nu}_e + \mathrm{p}^+ \longrightarrow \mathrm{e}^+ + \mathrm{n} \tag{1.1}$$

with the positron quickly annihilating, producing a detected photon pair. The neutron is absorbed by Cadmium

$$\mathrm{n} + {}^{108}\mathrm{Cd} \longrightarrow {}^{109m}\mathrm{Cd} \longrightarrow {}^{109}\mathrm{Cd} + \gamma \tag{1.2}$$

with a time delay providing a coincident second photon pulse.
At that time neutrinos were assumed to be massless, neutral, spin-$\frac{1}{2}$ fermions interacting weakly.
In 1962 Lederman, Schwartz and Steinberger[3] found a second type (*flavor*) of neutrinos associated with the muon (μ) in addition to the first one, where the first one produced only electrons in reaction 1.1. Later another neutrino flavor related to the third lepton (τ) was first discovered by the DONUT experiment[4]. DONUT observed interactions of the type

$$\nu_\tau \longrightarrow \tau + \mathrm{X} \tag{1.3}$$

followed by

$$\tau \longrightarrow \nu_\tau + \mathrm{Y} \tag{1.4}$$

and identified the short-lived τ by comparison of emission angles and track lengths.

1.2 Neutrino Oscillation

In the following years, a discrepancy was noticed between the measured flux of solar electron neutrinos and predictions based on the Standard Solar Model at that time,

puzzling the scientific community. This phenomenon of about two thirds of the neutrino flux seemingly missing was known as the Solar Neutrino Problem (SNP).
It was finally resolved experimentally through observations made by the Super-Kamiokande experiment[5] and the Sudbury Neutrino Observatory (SNO)[6].
SNO essentially consisted of a vessel containing 1000 t of pure D_2O surrounded by photomultiplier tubes. It detected multiple reactions involving neutrinos, some of them sensitive to neutrino flavor.
Starting with a deuteron (d), one charged current (CC) process observed was

$$\nu_e + \mathrm{d} \longrightarrow \mathrm{p}^+ + \mathrm{p}^+ + \mathrm{e}^-. \tag{1.5}$$

The resulting electron was detected through its Cherenkov radiation.
A concurrent neutral current (NC) process requiring incoming neutrinos was

$$\nu_\alpha + \mathrm{d} \longrightarrow \mathrm{p}^+ + \mathrm{n} + \nu_\alpha \tag{1.6}$$

with $\alpha = (e, \mu, \tau)$ for the three neutrino flavors. When the resulting free neutron is captured by a ^{2}H nucleus, a prompt gamma ray photon is emitted.

$$^2\mathrm{H} + \mathrm{n} \longrightarrow {}^3\mathrm{H} + \gamma(6.25\,\mathrm{MeV}) \tag{1.7}$$

Subsequent Compton electrons or e^-e^+ pairs moving through the vessel also lead to Cherenkov light detected with photomultipliers.
SNO therefore had independent ways to measure the ν_e flux and the total neutrino flux. Comparing these fluxes solved the SNP by proving that about two thirds of solar neutrinos emitted as ν_e are identified as ν_μ or ν_τ, when detected on earth.
This is referred to as neutrino oscillation. Contemporary descriptions of the neutrino propose two distinct types of eigenstates, flavor eigenstates m_α and mass eigenstates m_i with i=(1,2,3).
The description of the spatial propagation of neutrinos is based on their mass eigenstates, whereas the flavor eigenstate is relevant for the description of the weak interaction. A plain wave description of a neutrino in the i$^{\mathrm{th}}$ mass eigenstate at time t, impulse p_i and energy E_i gives

$$|\nu_i(t)\rangle = e^{-i(E_i t - p_i x)} \, |\nu_i(0)\rangle = e^{-i\Phi_i} \, |\nu_i(0)\rangle \, . \tag{1.8}$$

The phase Φ_i relates m_i to its propagation through

$$E_i = \sqrt{m_i^2 + p_i^2} \approx p_i + \frac{m_i^2}{2p_i}. \tag{1.9}$$

[1]For a different j$^{\mathrm{th}}$ mass eigenstate $|\nu_j\rangle$ usually $p_i = p_j$ or $E_i = E_j$ is assumed, which in general is not Lorentz invariant. It will nevertheless be assumed here for

[1]Expressions are given in natural units $c = \hbar = 1$ throughout this entire thesis, unless stated otherwise.

simplicity. Ultra-relativistic neutrinos then justify $L \approx t$ as well as

$$E \coloneqq E_i \approx p_i \gg m_i \forall i. \tag{1.10}$$

The phase difference therefore varies with L approximately like

$$\Phi_i - \Phi_j \approx \frac{m_i^2 - m_j^2}{2E} L = \frac{\Delta m_{ij}^2}{2E} L. \tag{1.11}$$

The mass eigenstate relates to the flavor eigenstate α, in which the neutrino is taking part in the weak interaction, by a transformation

$$|\nu_\alpha\rangle = \sum_i U_{\alpha i}^\star |\nu_i\rangle \tag{1.12}$$

U is a 3x3 unitary matrix named after B. Pontecorvo, Z. Maki, M. Nakagawa and S. Sakata (PMNS)[7]. For illustration purposes, suppose there are only two mass and flavor eigenstates and U is parameterized such that

$$\begin{pmatrix} |\nu_e\rangle \\ |\nu_\mu\rangle \end{pmatrix} = \begin{pmatrix} cos(\theta) & sin(\theta) \\ -sin(\theta) & cos(\theta) \end{pmatrix} \begin{pmatrix} |\nu_1\rangle \\ |\nu_2\rangle \end{pmatrix}. \tag{1.13}$$

The probability of a ν_α to be detected as ν_β is therefore related to the phase difference of mass eigenstates which varies with propagation distance (equation 1.11).

$$\begin{aligned} P_{\alpha\to\beta}(t) = |\langle \nu_\beta(0)|\nu_\alpha(t)\rangle|^2 = \left| \sum_{j,i} \langle \nu_j(0)| U_{\beta j} U_{\alpha i}^\star |\nu_i\rangle \right|^2 = \\ \sum_i |U_{\alpha i}|^2 |U_{\beta i}|^2 + \sum_{i\neq j} U_{\alpha j} U_{\beta j}^\star U_{\alpha i}^\star U_{\beta i} e^{-i(\Phi_i - \Phi_j)t} \end{aligned} \tag{1.14}$$

In the two neutrino case this equals

$$P_{\alpha\to\beta}(L) = sin^2(2\theta) sin^2\left(\frac{\Phi_i - \Phi_j}{2}\right) \approx sin^2(2\theta) sin^2\left(\frac{\Delta m_{12}^2}{4E} L\right). \tag{1.15}$$

adopting the approximation in equation 1.11.
The derivation is similar for three neutrino generations. Conveniently a parameterization characterized by three mixing angles (θ_{12}, θ_{13}, θ_{23}), one CP-violating phase (δ) and two phases ($\alpha_{1/2}$) irrelevant for Dirac neutrinos, is chosen.
Since oscillation of neutrinos has been observed, at least two of the masses m_i are non-zero. This means that neutrinos are not compatible with the standard model (SM) prediction of massless particles. Values of m_i are not accessible to oscillation experiments, as all transition probabilities depend only on Δm_{ij}^2.

1.3 Neutrino Nature

As of today, neutrinos are thought to be either Dirac or Majorana particles. When Majorana by nature, there is no way to distinguish antineutrinos from neutrinos, they would be their own antiparticles.
Ways to test this hypothesis involve the observation of a particular process called double beta decay.

$$(\mathrm{A}, \mathrm{Z}) \longrightarrow (\mathrm{A}, \mathrm{Z}+2) + 2\,\mathrm{e}^- + 2\,\bar{\nu}_e \tag{1.16}$$

As it is usually very rare, it can practically only be observed in case the single beta-decay is energetically forbidden. Therefore, typically atoms with very long half-life periods of $T_{1/2} > 10 \times 10^{19}\,\mathrm{yr}$ are employed experimentally.
Only for Majorana neutrinos a second kind of double beta decay ($0\nu\beta\beta$) emitting no neutrinos is possible.

$$(\mathrm{A}, \mathrm{Z}) \longrightarrow (\mathrm{A}, \mathrm{Z}+2) + 2\,\mathrm{e}^- + \mathrm{Q}_{\beta\beta} \tag{1.17}$$

This process is also violating lepton number conservation, which is forbidden in the SM.
The materials used experimentally for $0\nu\beta\beta$ decay search include ^{76}Ge (GERDA) and ^{136}Xe (EXO, KamLAND-Zen). The search consists of looking for double beta decays by measuring the sum of emitted electron energies. If the electron pair is emitted back-to-back and its sum of kinetic energies agrees with the total energy emitted $Q_{\beta\beta}$, a $0\nu\beta\beta$ decay is found. The kinetic energy of the daughter nucleus is negligible.
The GERDA experiment[8] consisted of a large amount of ^{76}Ge resulting in a high exposure of $127.2\,\mathrm{kg}\cdot\mathrm{yr}$. For ^{76}Ge the energy difference is $Q_{\beta\beta} = 2039\,\mathrm{keV}$. Germanium detectors were used for energy measurement.
GERDA set a limit (90 % CL) on the half-life of

$$T_{1/2}^{0\nu\beta\beta} = \left(G|\mathcal{M}|^2\langle m_{\beta\beta}\rangle^2\right)^{-1} > 1.8 \times 10^{26}\,\mathrm{yr}. \tag{1.18}$$

G is a phase space factor, $\mathcal{M}$ the nuclear matrix element and $\langle m_{\beta\beta}\rangle$ the effective Majorana neutrino mass. GERDA didn't find any evidence for Majorana neutrinos, the nature of neutrinos still remains undetermined.
Equation 1.18 can, under the assumption of light Majorana neutrinos dominating the decay process, be converted into an upper limit[8] (90 % CL) on

$$\langle m_{\beta\beta}\rangle = \left|\sum_i U_{ei}^2 m_i\right| < 79 - 180\,\mathrm{meV}. \tag{1.19}$$

The large range stems from the uncertainties of matrix elements involved.
This kind of experiment is consequently also sensitive to m_i using the mass differences measured by oscillation experiments and PMNS matrix elements.

1.4 Cosmological Limits

The values of the neutrino masses have significant impact on a number of cosmological observations. An effect accessible to observation is the impact on large scale structure (LSS) formation.
The neutrino density in the universe compared to the critical density ρ_c is

$$\Omega_\nu = \frac{\sum_i m_i n_i}{\rho_c} = \frac{\sum_i m_i}{h^2 \cdot 94\,\mathrm{eV}} \tag{1.20}$$

with number densities n_i and the Hubble parameter h.
An upper limit on Ω_ν comes from LSS surveys measuring spacial matter distribution in the universe. As neutrinos travel through space, they wash out mass perturbations on scales much smaller than their free streaming length. The correlations of the spacial distribution of matter in the universe, described by the matter power spectrum, are suppressed for small distances with larger Ω_ν. Cosmological observations yield an upper limit of the neutrino density of

$$0.1\,\% < \Omega_\nu < 0.5\,\%. \tag{1.21}$$

The lower limit comes from the lowest possible value of the sum $\sum_i m_i$ based on the measured mass splittings $\Delta m^2_{12} < \Delta m^2_{13} \approx \Delta m^2_{23}$.
As the signs of Δm_{ij} are not known, it is however not clear which ordering of neutrino masses is realized in nature. The *normal ordering* means $m_1 \approx m_2 < m_3$, the *inverted order* places m_3 below the other two mass eigenstates. The minimum value for the sum in the case of normal ordering is $\sum_i m_i > 58\,\mathrm{meV}$.
When combining results from a number of different cosmological observations, more stringent limits on neutrino masses can be obtained. The most constraining limits are placed at (95 % CL)[9]

$$0.058\,\mathrm{eV} < \sum_i m_i \lesssim 0.09\,\mathrm{eV}. \tag{1.22}$$

This already puts tension on the inverted ordering which requires $\sum_i m_i > 0.11\,\mathrm{eV}$.
Most of these inferences make use of the ΛCDM model in some form, as it is the standard model of cosmology. The simplest form of ΛCDM model is based on six cosmological parameters. Therefore, a dedicated measurement, independent of cosmological parameters unaccessible to particle physics experiments, is desirable.

1.5 Beta Decay Kinematics

Experiments relying on observations of beta decays, in contrast, yield results independent of neutrino nature and cosmological models.

The beta minus decay is described by the following formula.

$$\mathrm{n} \longrightarrow \mathrm{p}^{+} + \mathrm{e}^{-} + \bar{\nu}_e + \mathrm{Q} \tag{1.23}$$

Q is the energy released, which is then shared between the three products. The massive neutrino carries at least m_{ν_e} consequently reducing the energy available to the other particles. A measurement of the maximum kinetic energy of the electron is therefore sensitive to the electron neutrino mass

$$m_{\nu_e}^2 = \sum_i |U_{ei}|^2 m_i^2. \tag{1.24}$$

With Fermi's golden rule the differential spectrum of the emitted electron is determined as

$$\begin{aligned}\frac{d\Gamma}{dE} = \frac{G_F^2 cos^2(\theta_C)}{2\pi^3} |\mathcal{M}_{nuc}|^2 F(Z,E)\sqrt{(E+m_e)^2 - m_e^2}(E+m_e)\cdot \\ \sum_{i,j} |U_{ei}|^2 P_j \epsilon_j \sqrt{\epsilon^2 - m_i^2}\Theta(\epsilon_j - m_i)\end{aligned} \tag{1.25}$$

$$\epsilon_j = Q - E_{rec} - E - V_j. \tag{1.26}$$

G_F is the Fermi constant, θ_C the Cabibbo angle. $\mathcal{M}_{nuc}$ denotes the nuclear matrix element. The Fermi function F accounts for the interaction of the outgoing electron with the daughter nucleus of nuclear charge number Z. An illustration of the neutrino mass impact near the endpoint is shown in figure 1.1. Since the observable is the neutrino mass squared, results are often given for the squared mass value.
In case the beta decay happens inside atoms or molecules, V_j refers to the energy of the j^{th} rotational-vibrational excited state of the daughter molecule, P_j to the corresponding transition probability.

Tritium Within about the last thirty years a few neutrino experiments used T_2 tritium as beta decay source. The most recent ones being the experiments in Troitsk[10], Mainz[11] and the Karlsruhe TRItium Neutrino experiment (KATRIN). The following decay is observed.

$$\mathrm{T}_2 \rightarrow \mathrm{THe}^{+} + \mathrm{e}^{-} + \bar{\nu}_e + \mathrm{Q} \tag{1.27}$$

A endpoint E_0 is defined as

$$E_0 = Q - E_{rec}. \tag{1.28}$$

When observing tritium decays with electron energies close to the endpoint, the recoil of the THe^{+} molecule is nearly constant ($E_{rec} = 1.72\,\mathrm{eV}$).
There are a few arguments in favor of using tritium for this kind of experiments.

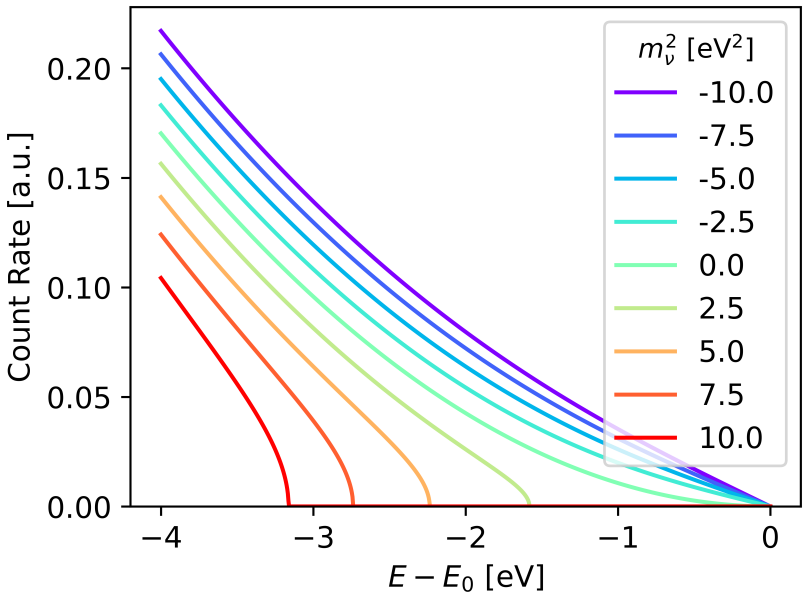

Figure 1.1: Electron spectrum for different neutrino masses near the endpoint following equation 1.25. No excited states of the daughter molecule were considered.

- Tritium beta decays are superallowed, which implies that the nuclear matrix element does not depend on the electron energy.
- Its half-life $T_{1/2} = 12.3\,\mathrm{yr}$ is rather short, making a high activity measurement feasible.
- Tritium decays allow relatively easy calculation of the daughter's final state energies and the corresponding probabilities (V_j, P_j) through its simple shell structure.
- The endpoint $E_0(T_2) \approx 18.6\,\mathrm{keV}$ is very low, so that a ppm precision high voltage energy filter for electrons near the endpoint can be realized.

The most strict limit from beta decay experiments was set by the KATRIN collaboration[12] at $m_\nu < 0.8\,\mathrm{eV}$ (90 % CL).

Chapter 2

KATRIN Experimental Setup

The KATRIN experiment[13][14] is set up at the Karlsruhe Institute of Technology in Karlsruhe, Germany. The parts of the beamline containing significant amounts of tritium are located within the facilities of the Tritium Laboratory Karlsruhe. Measurements started in 2018 and are ongoing.

2.1 Tritium Source

The *windowless gaseous tritium source* (WGTS) is located at section b) in the beamline (figure 2.1). It is the source of tritium beta decay electrons for the KATRIN experiment.
As windows would affect electron transmission by introducing additional scattering and absorption, the WGTS is realized as an open tube of about 10 m length and 90 mm inner diameter. During operation gaseous tritium is transversely injected at its center, T_2 molecules then diffuse through the WGTS. Turbo molecular pumps (TMPs) installed at the beam tube's front and rear end reduce the further flow of

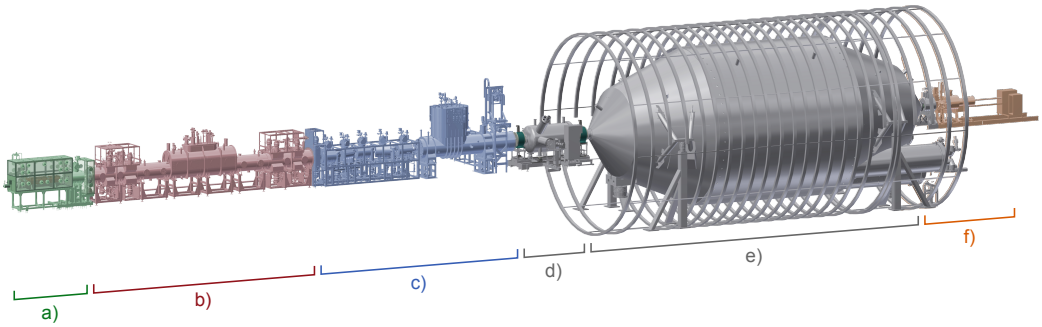

Figure 2.1: Beamline of the KATRIN experiment. a) rear section (2.6), b) tritium source (WGTS, 2.1), c) transport section (2.2), d) pre-spectrometer (2.3), e) main spectrometer (2.3), f) detector section (2.4). Figure by Leonard Koellenberger.

gas through the system by a factor of about 200[14]. A closed loop system connected with said pumps and additional ports in the transport section is employed for tritium recovery, temperature and pressure control, purification and monitoring.
The gas mixture in the WGTS consists of $> 95\,\%$ T_2, the remainder almost entirely consisting of DT and HT, and is kept at a temperature of $30 - 100\,\mathrm{K}$ depending on the specific measurement mode.
Resulting from beta decays of tritium happening in the WGTS, electrons are emitted. The beamline is surrounded by magnets generating magnetic fields in a longitudinal direction to guide charged particles through the entire setup. The magnetic field strength is about $2.51\,\mathrm{T}$ in the WGTS region.

2.2 Transport Section

The *transport section* is connected directly to the WGTS upstream (section c) in figure 2.1). Its purpose is to adiabatically guide beta electrons towards the main spectrometer along magnetic field lines and further remove unwanted particles from the system.
The flow of neutral molecules towards the main spectrometer is reduced by combining TMPs in the WGTS section and another set of TMPs installed in the *differential pumping section* (DPS) of the transport section by many orders of magnitude. The DPS section alone achieves a flow reduction better than four orders of magnitude[15]. The flow is further reduced employing cryo-sorption pumps by the cryogenic pumping section in the transport section by a design value of another seven orders of magnitude[13]. The finned inner surface of this section's beam tube is cooled to $3\,\mathrm{K}$. It is further aided by two chicanes consisting of sections tilted by $20\,\mathrm{deg}$ and $15\,\mathrm{deg}$ blocking a line-of-sight path of flight in the differential and crypo pumping section respectively .
As charged tritium ions are also bound to follow magnetic field lines, additional measures have to be taken for their removal. Ring electrodes at a positive potential $(5 - 200\,\mathrm{V})$[13] combined with dipole electrodes in the DPS section remove positive ions via an $E \times B$ drift.

2.3 Pre-Spectrometer and Main Spectrometer

The pre-spectrometer at section d) of the beamline (figure 2.1) defines the region of maximum magnetic field strength $B_{max} = 4.2\,\mathrm{T}$ in the KATRIN experiment. B_{max} determines the energy filter's resolution and the maximum acceptance angle for electrons emmited in the WGTS as described in section 2.5.1.
The main spectrometer is located in section e) of the depicted beamline in figure 2.1. Its purpose is to implement the MAC-E energy filter design ()section 2.5.1) in ultra

high vacuum conditions.
This is achieved with a high precision electric negative retarding potential combined with a low magnetic field inside the main spectrometer.
Power supplies define a retarding potential between the main spectrometer and the WGTS for absolute voltages as high as 35 kV at a ppm precision level[16]. Absolute voltages up to 35 kV are not required for investigation of the β-spectrum, but for calibration measurements using ^{83m}Kr. Throughout this thesis the sign of the retarding poential is often omitted for convenience.
The configuration of magnetic field lines is set to be either symmetric or asymmetric with respect to the oval spectrometer shape. The symmetric field configuration is realized by setting magnets at both ends of the main spectrometer to the same field values. The asymmetric *shifted analyzing plane* (SAP) configuration is precisely tuned by adjusting individual currents of 16 concentrical coils along the length of the entire main spectrometer. The SAP setting shifts the spatial region (*analyzing plane*) of lowest magnetic field and highest absolute electric potential difference (with respect to the WGTS) further downstream towards the detector section. This is done to reduce the main background component, which depends on the volume of the flux tube after the analyzing plane.

2.4 Detector Section

The *detector section* is located at section f) in figure 2.1.
In the detector section a post acceleration voltage for the incoming electrons is supplied. This potential of about 10 kV accelerates negative particles further upstream and therefore reduces the fraction of electrons lost due to backscattering after hitting the entrance window of the *focal plane detector* (FPD). This also suppresses background electrons that emerge close to the FPD, since they are not accelerated by the full post acceleration potential. The FPD is a silicon drift detector consisting of 148 equal size p-i-n diode arrays (*pixels*) on a silicon wafer. The FPD segmentation is depicted in figure 2.2. Not all pixels are used for the neutrino mass analysis. The detector has a 100 nm dead layer.
During operation the energy resolution of the FPD is not as critical, as the energy filtering is done with a MAC-E filter design and therefore only the measured number of counts in the FPD is needed.

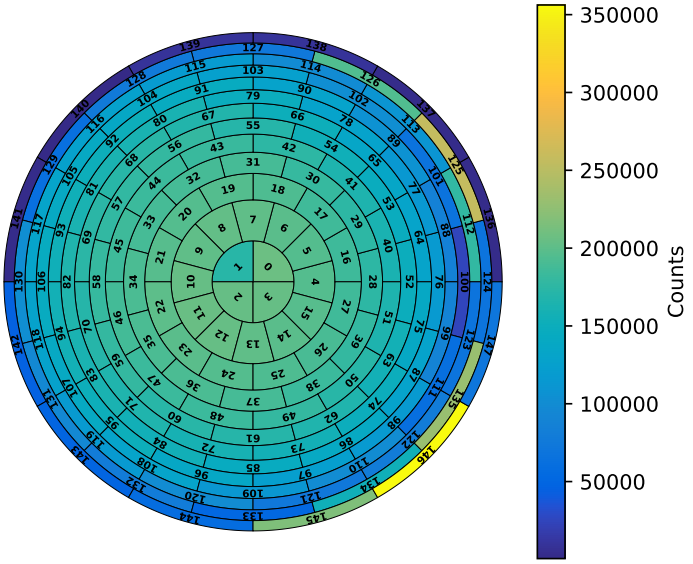

Figure 2.2: The focal plane detector (FPD) is a silicon wafer segmented into 148 pixels of equal area (44 mm^2). Shown is the distribution of counts for a measurement of the rear wall spectrum, summed over all retarding energy setpoints.

2.5 Model of the Integral Spectrum

2.5.1 Energy Filter

The energy spectrum of beta decay electrons follows equation 1.25.
In order to not require a precise energy resolution at keV energies, which is not possible with current detector technology, the differential spectrum is integrated and filtered in energy before reaching the detector. For that a *magnetic adiabatic collimation with electrostatic* (MAC-E) filter schematically shown in figure 2.3 is employed. The MAC-E filter design comprises an electric potential acting as an energy filter and a magnetic field with field lines parallel to the electrons' path of flight. Charged particles are magnetically guided to move in a cyclotron motion around the field lines. Since the magnetic field is only slowly changing with respect to the electrons' movement, their magnetic moment

$$\mu = \frac{m_e v_\perp^2}{2B} \propto \frac{v_\perp^2}{B} = const \tag{2.1}$$

is a transverse adiabatic invariant. $v_\perp$ is the electron velocity perpendicular to the magnetic field lines, B the magnetic field, m_e the electron mass.

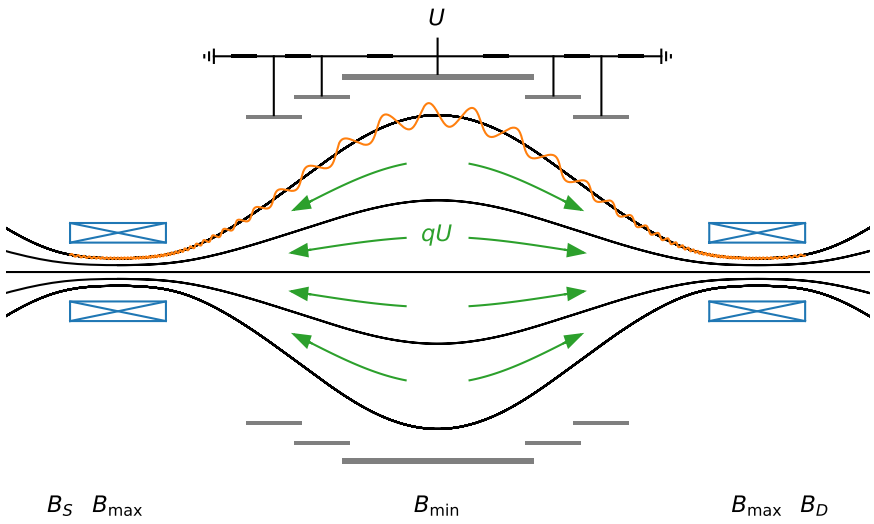

Figure 2.3: MAC-E filter design as realized in the KATRIN main spectrometer (2.5.1). A negative electric potential with respect to the source of beta decay electrons up to $U \approx -35\,\mathrm{keV}$ is applied. The magnetic field, smallest inside the spectrometer, aligns the electrons' perpendicular velocity component making the energy filter more efficient. Figure by Christian Karl, adapted from [17].

For an electron starting in a source magnetic field B_s with velocity $v_{\perp,s}$, reaching a maximum magnetic field B_{max} at a velocity $v_{\perp,max}$ therefore follows

$$v_{\perp,max}^2 = \frac{B_{max}}{B_s} v_{\perp,s}^2. \tag{2.2}$$

Using the first relation of the following expression for the total energy

$$E = E_\perp + E_\parallel = \frac{1}{2} m v_\perp^2 + \frac{1}{2} m v_\parallel^2 = \frac{m v_\parallel^2}{2}(1 + tan^2(\theta)) = const \tag{2.3}$$

equation 2.2 becomes

$$\frac{2E}{m} - v_{\parallel,max}^2 = \frac{B_{max}}{B_s}\left(\frac{2E}{m} - v_{\parallel,s}^2\right). \tag{2.4}$$

Electrons are reflected when in the region of high magnetic field their $v_{\parallel,max} = 0$. Inserting this condition in equation 2.4 gives

$$v_{\parallel,s}^2 = \frac{2E}{m}\left(1 - \frac{B_s}{B_{max}}\right). \tag{2.5}$$

Finally, exploiting the trigonometric relation in equation 2.3 for the starting angle θ of the electron path of flight with respect to the source magnetic field lines we arrive at

$$\theta_{max} = sin^{-1}\left(\sqrt{\frac{B_s}{B_{max}}}\right). \tag{2.6}$$

θ_{max} represents the maximum starting angle for electrons emitted in the source to not be reflected in the region of maximum magnetic field and is therefore called acceptance angle. By defining the magnetic fields in KATRIN ($B_s = 2.51\,\mathrm{T}$ in the WGTS, $B_{max} = 4.2\,\mathrm{T}$ at the pre-spectrometer) it is chosen to be about $\theta_{max} \approx 50.5°$. This is optimized to, on the one hand obtain a high luminosity, on the other hand exclude electrons traveling a long distance through the WGTS potentially undergoing a large number of scattering events.
The region inside the main spectrometer where the magnet field is weakest and the full voltage of about $-18.6\,\mathrm{kV}$ with respect to the source is applied, is called *analyzing plane*. At the analyzing plane, oriented pependicular to the beamline, a magnetic field B_{ana} as low as about $6.3\,\mathrm{G}$ is achieved. Therefore, according to equation 2.1 the perpendicular component of the electron velocity almost vanishes, leaving the entire kinetic energy in the parallel direction. This allows the full electric potential to take effect, resulting in precise energy filtering.
As an accelerating voltage is applied after the analyzing plane, to first approximation almost all of the electrons passing the analyzing plane reach the detector, regardless of their surplus energy.
The detector counting incoming electrons is therefore measuring the count rate of the integral electron spectrum.
Neglecting scattering of electrons in the source the transmission probability of electrons with kinetic energy E at a retarding potential U can be written as[18]

$$T(qU,E) = \begin{cases} 0 & E < qU \\ \dfrac{1 - \sqrt{1 - f\dfrac{B_s}{B_{ana}}\dfrac{E-qU}{E}}}{1 - \sqrt{1 - \dfrac{B_s}{B_{max}}}} & qU \le E \le qU\dfrac{fB_{max}}{fB_{max} - B_{ana}} \\ 1 & E > qU\dfrac{fB_{max}}{fB_{max} - B_{ana}} \end{cases} \tag{2.7}$$

with the electron charge q and the factor

$$f = \frac{\frac{E - qU}{m_e} + 2}{\frac{E}{m_e} + 2}. \tag{2.8}$$

The shape of the transmission function is illustrated in figure 2.4.
The width of the non-constant part of the transmission function is read off as

$$\Delta E = qU \frac{B_{ana}}{\frac{(E - qU)/m_e + 2}{E/m_e + 2} B_{max} - B_{ana}} \approx E \frac{B_{ana}}{B_{max}} \frac{E/m_e + 2}{2}. \tag{2.9}$$

To obtain a sharp energy resolution (i.e. small ΔE) it is generally desirable to set a very small magnetic field B_{ana}.
Conservation of flux,

$$B \cdot A = const \tag{2.10}$$

with magnetic field B in area A, and high magnetic fields ($3.6 - 6\,\mathrm{T}$) on the small area of the FPD (90 mm diameter) requires a large area in the analyzing plane inside the main spectrometer[18]. That is the reason why the main spectrometer vessel has a large diameter of up to 9.8 m.

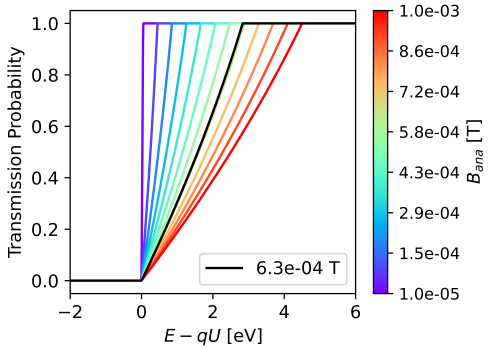

Figure 2.4: Transmission probability of a MAC-E filter described in equation 2.7. Magnetic field values are set to $B_s = 2.51\,\mathrm{T}$, $B_{max} = 4.2\,\mathrm{T}$

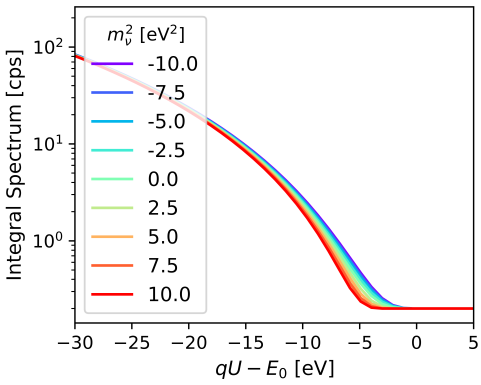

Figure 2.5: Effect of the MAC-E filter transmission function on the integral spectrum measured in the FPD. Scattering in the source was not considered in this plot.

2.5.2 Scattering

As beta decays happen inside the WGTS, the emitted electrons are subject to scattering processes with tritium gas molecules. When i-fold inelastic scattering occurs, electrons lose energy according to an energy loss function $f_i(E)$[19]. The probability of i-times inelastic scattering $P_{inel,i}$ depends on the emission angle θ and the point of emission in the source z. $z \in [0,1]$ is defined with a constant differential amount of traversed gas towards in a longitudinal direction towards the FPD. To first order approximation these two parameters determine the amount of gas the electrons traverse. Assuming that the angle θ doesn't change after scattering, the probability is approximated as

$$P_{inel,i}(z,\theta) = \left(\frac{z \cdot \rho d}{cos(\theta)}\right)^i \frac{\sigma_{inel}^i}{i!} \cdot exp\left(-\frac{z \cdot \rho d \cdot \sigma_{inel}}{cos(\theta)}\right) \tag{2.11}$$

$\sigma_{inel} = 3.456 \times 10^{-18}\,\mathrm{cm}^2$ is the inelastic scattering cross section for T_2[13] and ρd the column density. The elastic cross section can be neglected, as it is a magnitude smaller than σ_{inel} and the related energy loss strongly peaked in the $\lesssim 10\,\mathrm{meV}$ engery range[18]. The column density ρd is the density of tritium molecules integrated over the source length. The measured beta decay signal scales with ρd, but will reach an asymptotic maximum, as also the probability of inelastic scattering increases with ρd. Towards higher column density values the corresponding systematic uncertainties are increasing as well, by that defining an optimal value for ρd[13].
To describe the entire source, the scattering probabilities are integrated over z and θ. θ_{max} is the acceptance angle as described in equation 2.6.

$$P_i = \frac{1}{1 - cos(\theta_{max})} \int_0^{\theta_{max}} d\theta \; sin(\theta) \int_0^1 dz \; P_{inel,i} \tag{2.12}$$

Combining the description of the MAC-E filter transmission function $T(qU,E)$ with the energy loss due to scattering results in a convolution for the response function

$$R(qU,E) = \int_0^{E-qU} dE' \; T(qU, E-E') \sum_{i=0}^{\infty} P_i(E') \cdot f_i(E'). \tag{2.13}$$

When the differential spectrum is integrated over the response function, the result is the count rate as seen in the FPD.

$$I(qU) = N_{eff} \cdot \Omega \cdot \epsilon_{det} \int_{qU}^{E_0} dE \; R(qU,E) \frac{d\Gamma}{dE}(E) + B \tag{2.14}$$

N_{eff} is the effective number of tritium molecules, $\Omega = sin^2\left(\frac{\theta_{max}}{2}\right)$ the relevant solid angle pointing towards the FPD and $\epsilon_{det} \approx 95\,\%$ the assumed constant detector efficiency. B is an empirical background rate that is constant near the endpoint.

2.6 Rear Section

The rear section is located at the rear end of the experiment corresponding to section a) of the beamline in figure 2.1.

2.6.1 Design

Electron Gun The angular selective electron gun (eGun) setup located at the very end is used to emit electrons traveling through the entire beamline for characterization measurements. The mono-energetic electron beam (18 790 eV) is attenuated by scattering in the WGTS and measured with the FPD afterwards. During this measurement the energy filter is set to retarding voltages $5 - 200$ eV below the eGun electron energy, thus blocking all WGTS beta decay electrons. It therefore allows a direct measurement of the WGTS column density. This type of column density evaluation is carried out about once a week.

Rear Wall Following the eGun downstream is the *rear wall* (figure 2.6). The rear wall (RW) is a gold coated stainless steel disk with a diameter of 146 mm pointing towards the WGTS. A central hole of 5 mm diameter allows the eGun beam to pass through. On the back side a titanium plate is attached, with heating wires mounted on the titanium plate. Placed next to these are temperature sensors for monitoring. A small motor is located underneath the RW to automatically close its central hole, but it is currently not in use.
The RW is installed such that there is no direct electrical connection to the beam tube. A voltage of ± 500 V (*RW voltage*) can be applied to the RW surface.
A picoamperemeter provides a way to measure the current flow to the RW.
A quartz window mounted at a 55° angle pointing at the RW surface can be used to illuminate the RW with UV light.
The RW is not cooled and therefore operated at room temperature, the magnetic field in the region of the RW chamber is $B_{RW} = 1.23$ T.

BIXS Monitor The beta-induced X-Ray spectrometry (BIXS) detector system consists of two off-axis silicon drift detectors pointed at the RW. They are detecting X-Ray photons generated as Bremsstrahlung when electrons are absorbed in the RW gold layer. These electrons originate from the WGTS or beta decays on the RW surface. It therefore provides a way to measure changes of the source activity. The

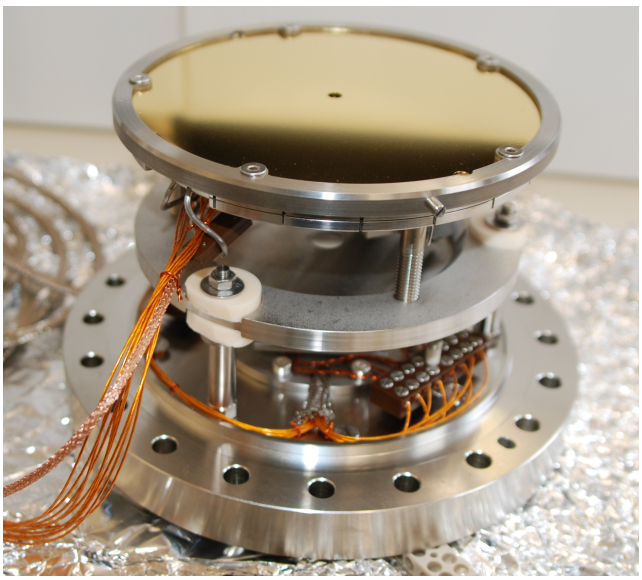

Figure 2.6: KATRIN rear wall before assembly. Picture taken by Alexander Jansen.

feasibility of monitoring the WGTS beta decay activity at the 0.1 % level has been demonstrated[20][21].

2.6.2 Rear Wall Tasks

The first task of the RW is to provide a surface for removing unwanted charged and neutral particles from the system.
Magnetic field lines run longitudinally through the entire beamline ending on the FPD and the RW. Charged particles are magnetically guided to move in a gyromotion along the field lines. After a beta decay inside the WGTS, an electron and a positive ion emerge. Half of the times the electron exits towards the rear end and is guided onto the RW surface. If the electron is emitted towards the main spectrometer, it might be reflected before or at the analyzing plane, depending on electron energy and retarding voltage. If reflected, it will usually follow the field lines back through the WGTS and also reach the RW surface. In case scattering occurs after entering the main spectrometer there can be conditions in which the electron is trapped in the system. Also a fraction of tritium ions created by beta decays and ionization reaches the RW. Particles guided to the RW surface are absorbed and thus removed from the system.
The second task of the RW is to provide a potential to define the source potential and optimize plasma homogeneity[22].

In the WGTS there is a large number of charged particles defining a plasma, as well as neutral tritium gas. Every beta decay electron produces 15 secondary electrons on average[23]. The plasma defines the starting potential of beta decay electrons emitted by neutral molecules. The longitudinal conductivity towards the RW of the beamline is high for electrons. For ions there is also a small non-negligible fraction transported in the radial direction to the beam tube wall. The potential in front of a surface is, for charged particles in contact with it, also depending on the surface material work function. Taking work function differences between RW and beam tube into account, small RW potentials are effectively transported to the plasma.

2.6.3 Systematics Associated with the Rear Wall

As the plasma potential is coupled to the RW potential, and suboptimal rRW voltages lead to inhomogeneities of the plasma, the systematic uncertainty associated with the plasma contains a rear wall dependency.
Another systematic uncertainty is related to the bombardment of the rear wall surface with electrons and ions. By that, radioactive molecules are formed on or inside the RW. Neither the exact mechanism nor the types of molecules created is precisely known. These molecules undergo beta decays and produce an integral electron spectrum, also observed in the FPD, that is different from a T_2 spectrum. It is therefore detected as a superimposing beta decay background spectrum in neutrino mass data. An exemplary comparison of this RW spectrum is shown in figure 2.7.
The beta decay activity originating at the RW increases monotonically during tritium circulation. The exploration of this variable background spectrum as well as its correction is the main focus of this thesis and described in chapters 3 and 4.

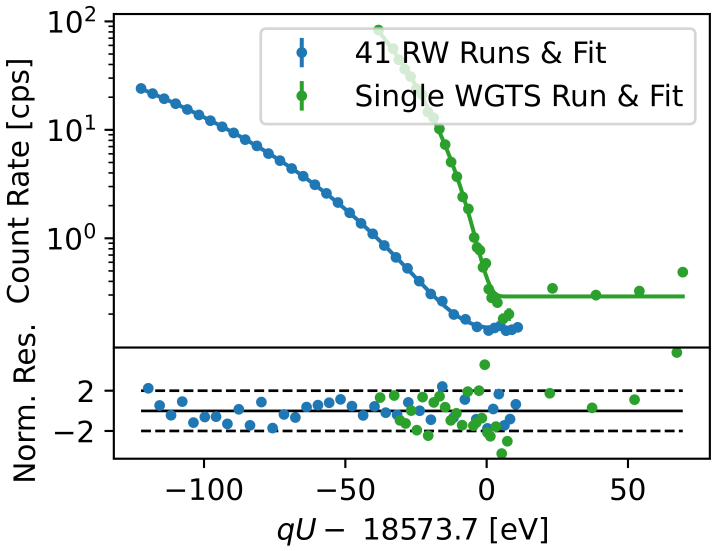

Figure 2.7: Comparison of a beta decay spectrum originating in the WGTS with a spectrum obtained only from the rear wall. Fits shown are T_2 spectra with endpoint, amplitude and flat background as fit parameters.

Chapter 3

Rear Wall Measurements and Tritium Final States Fit Analysis

3.1 Neutrino Mass Measurements

The measurements used for the neutrino mass analysis are taken in chunks of *beta scans*. A single beta scan consists of measurements at multiple retarding voltage setpoints (U). Each voltage configuration is kept constant for a predetermined time, depending on U defined by the *measurement time distribution* (MTD). See figure 3.2 for a graphical representation. In total one beta scan run contains about $2 - 4\,\mathrm{h}$ of measurement time.
Operation is organized in measurement campaigns of about three months length, denoted as (KATRIN neutrion mass) KnmX, with $X = (1, 2, 3, ...)$ in ascending order. See figure 3.1 for an overview. This thesis focuses on campaigns Knm3 to Knm5 measured from June 2020 to June 2021.

3.2 Rear Wall Neutrino Mass Bias

The bias caused by neglecting the presence of the RW background spectrum in the neutrino mass analysis was quantified by generating an Asmiov spectrum containing the WGTS spectrum and a RW background. This combined spectrum was subsequently fitted with only a WGTS spectrum.
At the RW activity on the average level of Knm4, the bias of the squared neutrino mass fit variable m_ν^2 is about $-0.02\,\mathrm{eV}^2$. It is approximately proportional to the RW activity. As KATRIN aims for a $0.2\,\mathrm{eV}$ neutrino mass sensitivity at $90\,\%$ CL, the RW is potentially inducing a significant bias. Hence it has to be taken account as a background spectrum for the neutrino mass analysis. A number of different approaches to achieve this are presented in sections 3.5 and 4.1.

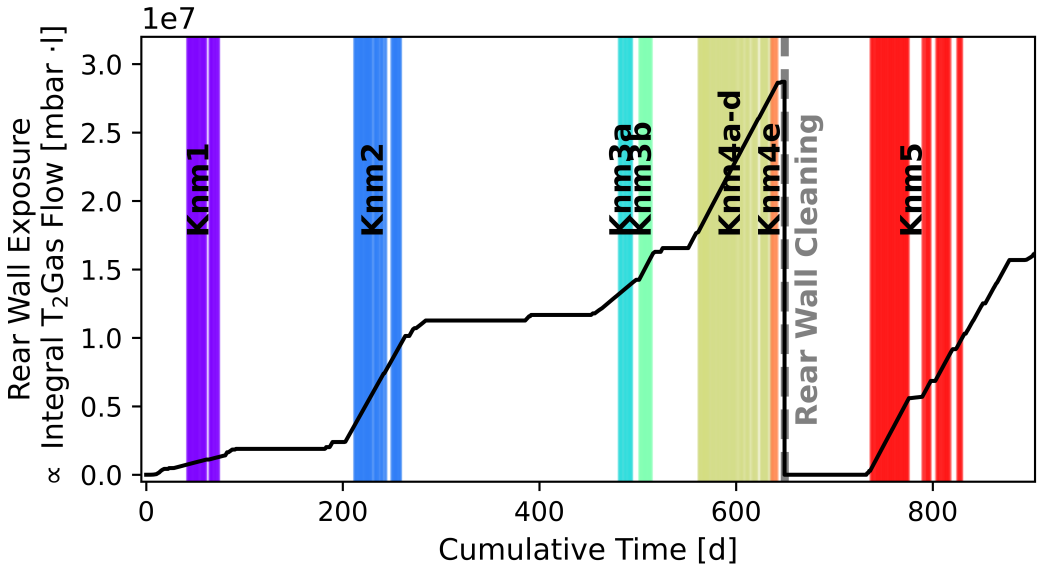

Figure 3.1: Rear wall exposure to tritium decays from the WGTS, proportional to the integral flow of injected tritium gas. It is therefore by convention reset to zero after the successful RW cleaning reduced the RW activity almost completely (see section 3.4). The time axis starts in February 2019. Colored bands indicate measurement time used in the neutrino mass analysis, i.e. maintenance breaks or e.g. periods with unstable slow control parameters are excluded.

3.3 Rear Wall Measurement Settings

As the RW spectrum superimposes the WGTS spectrum during beta scans, and is, also due to its low count rates, therefore hard to distinguish, dedicated RW measurement campaigns for RW characterization and monitoring are carried out at least once per three months neutrino mass campaign. The first one was done after Knm3 (see table A.1 for an overview). An example spectrum is shown in figure 2.7.
These *RW scans* make use of the experimental setup described in section 2, the measurement configuration only differs from beta scan settings in the following aspects.

- During RW scans the WGTS is empty. In contrast to measurements of beta scans, the RW electrons therefore don't scatter on tritium molecules in the source.
- The retarding voltage is varied according to a *flat* measurement time distribution (MTD) as depicted in figure 3.2. The MTD is different than during beta

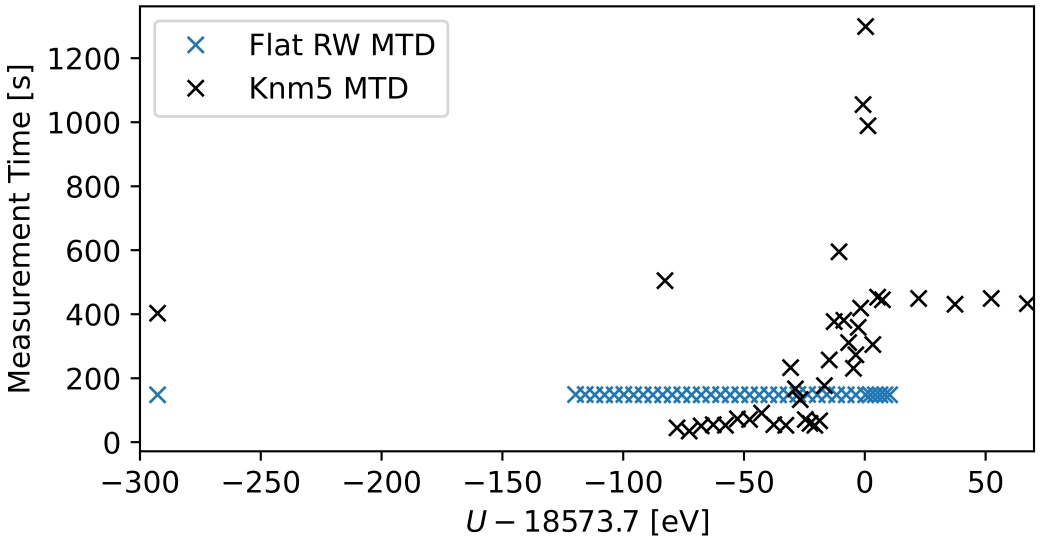

Figure 3.2: Comparison of the measurement time spent at each retarding voltage setpoint (measurement time distribution, MTD) of a neutrino mass measurement and a rear wall (RW) characterization run. Two retarding energy settings of the RW MTD are omitted in this plot: 16 976 eV and 17 176 eV with the same measurement times as the other RW points.

scans, since it is rather preferable to increase statistics by measuring far from the endpoint than spending time in the neutrino mass region where RW count rates are very low (see figure 2.7 for an example RW spectrum).

- The RW voltage during RW scans is not tuned to an optimal setpoint (see section 2.6.2) but kept fixed. The value is usually 0 V but has been set to different voltages for some scans. An overview of RW voltage configurations is depicted in figure 3.3.

3.4 Rear Wall Cleaning

The activity from the RW (*RW activity*) continuously increases with ongoing tritium circulation in the WGTS (see also section 2.6.3). A RW cleaning procedure was developed by Rudolf Sack to decrease the RW activity and by that reduce its impact on beta scans.

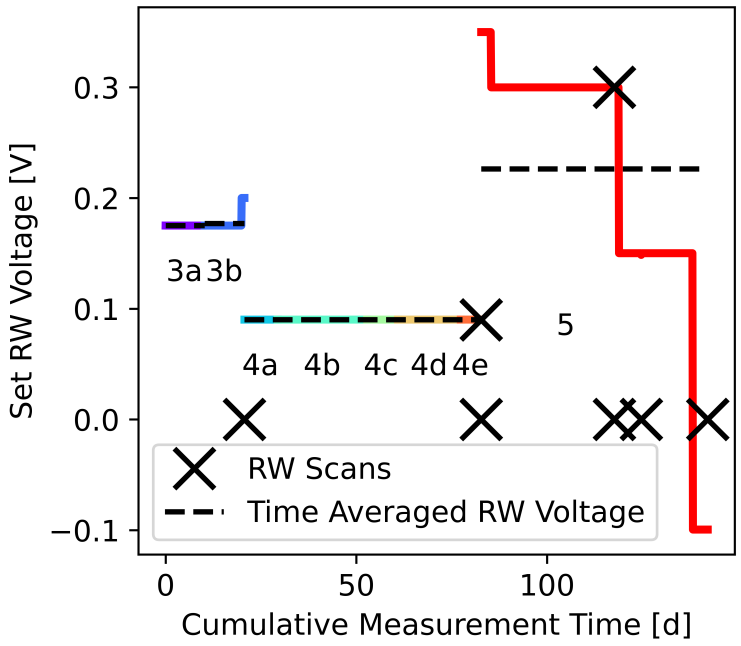

Figure 3.3: History of set rear wall voltages for campaigns Knm3 to Knm5. It was changed multiple times during Knm5 to compensate a drift of the RW workfunction. The black dashed lines indicate the time averaged RW voltage. The shown RW scans were all either done after neutrino mass campaigns had ended or during maintenance breaks.

The cleaning procedure leading to the fastest decrease of activity was found to be heating to 165 °C while treating the surface with ozone. Ozone is produced with UV-light irradiating oxygen gas inside the RW chamber.

$$\mathrm{O_2} \xrightarrow{\text{UV light}} 2\,\mathrm{O} \tag{3.1}$$

$$\mathrm{O} + \mathrm{O_2} \longrightarrow \mathrm{O_3}. \tag{3.2}$$

The ozone is then forming bonds with molecules of the contamination layer on the wall, resulting in effective desorption. The formed molecules and the ozone are subsequently removed by pumping. With the help of the Beta Induced X-Ray Spectrometry systems, changes of the X-ray intensity emitted by the RW are monitored while cleaning. This gives a way to evaluate the effectiveness of the cleaning procedure and obtain a live estimate on the relative reduction of the RW activity.
Cleanings were done after Knm4 and after Knm6, each reducing the RW activity by more than 95 %.

3.5 Tritium Final States Fit Procedure

The goal of the RW analysis is to provide a way to correct the neutrino mass analysis with the non-uniform background, posed by the RW integral spectrum, to get an unbiased m_ν^2 result. Therefore fits of the integral spectrum from RW scans are done to determine the RW spectral parameters. The RW background counts seen in the FPD during beta scans are estimated accordingly. Hereby the differences in measurement configuration listed in section 3.3, the correct scattering of RW electrons and the properties of the MAC-E filter are taken into account. The scattering differs from the scattering of WGTS electrons, as the RW electrons all traverse the entire WGTS, increasing the probability of scattering. The acceptance angle and the angle of RW electrons inside the WGTS is also different, since the magnetic field at the rear section is significantly lower ($B_{RW} = 1.23\,\mathrm{T}$) than in the WGTS. The estimations of RW count rates are added to the expected count rate (equation 2.14) from the WGTS in the neutrino mass fit.
As the RW spectrum shape is not precisely known, but is empirically seen to roughly resemble a T_2 beta decay spectrum with different endpoint (E_0), signal normalization and flat background, this model was taken as a baseline fit in this thesis. As it is based on the final states of T_2 it is called the *tritium final states fit* from here on. Assuming this modified T_2 spectrum, doesn't question the main features of the shape of the RW integral spectrum. Further investigations with less strict assumptions are described in the *systematics* section 4.1.
Combining the information gained from dedicated RW measurements and estimating corrections to cause no bias in the neutrino mass analysis relies on three different types of measurements and therefore a number of independent models.
The measurements that have to be considered are:

- *RW activity measurements* at 14 kV retarding voltage done with the help of the forward beam monitor[24] detector inside the transport section's beam tube. These are carried out non-regularly throughout neutrino mass campaigns.
- *RW scans* done in a configuration roughly resembling the beta scan measurements (see section 3.3 for details).
- *Beta scans* which the RW correction should be calculated for.

In the tritium final states fit analysis, based on these measurements, values for the T_2 spectrum endpoint and the signal normalization are required for correction of the RW background. A flat background seen in RW scans is assumed to not cause a non-uniform background during beta scans. A flat background is explicitly fitted in the neutrino mass analysis, corresponding fit values from RW scan fits are therefore

ignored in the RW analysis.
For some campaigns, the neutrino mass analysis combines groups of FPD pixels mapping very similar properties of the MAC-E filter to form *rings* or *patches*. The specific groups of pixels depend on the configuration of the MAC-E filter. If these rings or patches are used and consequently analyzed separately, the RW analysis is also required to provide ringwise or patchwise values as input for the RW correction.

3.5.1 Rear Wall Scan Fit Settings

Non-physical parameters used for fitting RW scans, that are not specified by the respective measurement configuration, should be consistent to allow comparison and combination of fit results. The chosen settings are described in the following.
As an integral tritium spectrum is fitted, a value for the column density is needed to base the value of the fitted spectrum normalization on. As there is no tritium inside the WGTS during RW scans, it doesn't correspond to a real value and can be chosen arbitrarily. It was chosen to be $3.75 \times 10^{21}\,\mathrm{m}^{-2}$. In the neutrino mass fit the column density value is set to the same physical value for beta scans and the RW correction. To compensate this slight difference between the physical value during beta scans and the arbitrary value set for RW scan fitting, scaling of the RW normalization result is required.
The same applies for fractions of molecule species in the tritium gas. They were chosen as follows ζ_{T_2}: 96 %, ζ_{HT}: 3 %, ζ_{DT}: 1 %, which is close to the real gas composition. It is summarized as tritium purity

$$\epsilon = \zeta_{T_2} + \frac{\zeta_{HT} + \zeta_{DT}}{2}. \tag{3.3}$$

Since count rates close to the T_2 endpoint are very low (see figure 2.7), measured rates at retarding voltages down to 18 455 eV were used for all tritium final states fits in this chapter.
Doppler broadening was not included, as the effect affects molecules on or inside the RW differently compared to tritium gas.

3.5.2 Models

Evolution of slow control parameters (e.g. RW voltage) and the RW activity during neutrino mass measurements, affecting the RW spectrum, must be taken into account by either the neutrino mass analysis or the RW analysis. It was chosen to leave this task largely to the RW analysis and only provide already corrected effective values describing the influence of the RW to plug into the neutrino mass fit. As for the neutrino mass analysis, determining physical properties of the RW is of interest just as far as they have any influence on neutrino mass measurements or are needed for

its description.
In the described analysis a number of different models and assumptions are employed as follows.

Intflow measurements Continuous monitoring of the integral flow (*intflow*) of tritium gas injected into the WGTS, allows relating each point in time to an intflow value i.e. an effective RW exposure.
The RW exposure is needed as the base of the RW activity model. Intflow values corresponding to a specific measurement are mapped by comparison of timestamps.

RW activity model During operation, a significant change in the spectral properties of the RW is assumed to only be induced by the circulation of tritium gas in the WGTS (RW exposure). No significant changes of the activity were observed as a result of longer pauses of tritium circulation.
The value of the RW activity, as seen in the RW activity measurement, $A(intflow)$, is therefore modeled as a function depending on intflow only. For that an appropriate smooth function is fitted to the data.

RW normalization model The rate in the RW activity measurement is assumed to be proportional to the RW normalization N in RW scans.
The factor of proportionality s is modeled to be constant between RW cleanings.

$$N = s \cdot A(intflow) \tag{3.4}$$

RW endpoint model A model yielding the endpoint of the RW spectrum $E_{0,eff}(intflow)$ throughout the neutrino mass campaign is needed, since RW scans obtain statistically different results each time. This model also has to account for the changing values of the RW voltage setpoint over the course of beta and RW scans. A non-zero RW voltage U_{RW} changes the RW starting potential and therefore directly shifts the RW endpoint. This was verified experimentally by Max Aker.

$$E_{0,RW}(U_{RW}) = E_{0,RW}(0\,\mathrm{V}) - U_{RW} \tag{3.5}$$

3.5.3 Rear Wall Endpoint Analysis

The models listed above are constructed sequentially.

3.5.3.1 Central Value

At first a fit is done yielding the RW activity obtained from RW activity measurements as a function of intflow $A(intflow)$.

Fits of RW scans combining counts from all pixels (*uniform* fits) are done to obtain the corresponding endpoint and signal normalization.
The scaling factor s mapping from $A(intflow)$ to the corresponding RW normalization is directly calculated with equation 3.4.
The endpoint of all RW scans in the considered time period is computed as weighted mean, taking the inverse variances as weights. To obtain the RW endpoint during each beta scan, this weighted mean is then shifted by the RW voltage set for that beta scan (equation 3.5). This yields an effective endpoint $E_{0,eff}(intflow_i)$ for the i^{th} beta scan at intflow $intflow_i$. An even more fine-graned approach taking into account the region of interest or the ordering of the measured retarding voltages is expected to only yield insignificantly different results.
For each beta scan included in the neutrino mass analysis, that the RW correction should be calculated for, its runtime T_i and $intflow_i$ as well as the scaling factor s is used to compute a weighting factor w_i:

$$w_i = s \cdot A(intflow_i) \cdot T_i \tag{3.6}$$

The value of w_i is approximately proportional to the number of electrons coming from the RW detected in the FPD during the i^{th} beta scan.
As the counts and runtimes of beta scans are all summed up for the neutrino mass analysis, beta scans containing a higher number of RW counts contribute more to the overall effective value of the RW properties. This is considered by computing the weighted mean of the $E_{0,eff}(intflow_i)$ values. With w_i being the weights, it is an effective RW endpoint weighted by RW counts.

$$E_{0,eff} = \frac{\sum_i E_{0,eff}(intflow_i) w_i}{\sum_i w_i} \tag{3.7}$$

3.5.3.2 Error Propagation

To compute the central value as well as an uncertainty on $E_{0,eff}$ based on equation 3.7, a Monte Carlo propagation technique is used. All values needed for the above models are sampled according to their corresponding uncertainties and best fit values and are used to compute the effective endpoint $E_{0,eff}$ via the method described above.
The uncertainties taken into account were the following:

Uncertainty of the RW activity model The uncertainty of the RW activity model is assumed to be contained in the covariance matrix of the fitted parameter values describing $A(intflow)$. Therefore model parameter values are sampled from that covariance matrix and the corresponding best fit values.

Uncertainty of the RW normalization model The uncertainties of the normalization model stem from the fit values' uncertainties of the normalizations of the RW scan fit results. For each RW scan fit, values for the normalization are sampled from their covariance matrix and the best fit values. As there is usually more than one RW scan per neutrino mass campaign, these sampled values and the fit uncertainties are used in a least squares fit to the RW activity model, yielding a value for the scaling factor s.

Uncertainty of the RW endpoint model The uncertainties on the endpoints of the uniform fits to the RW scans are incorporated by sampling endpoint values for each RW scan from the corresponding Gaussian distribution given by standard deviation and best fit value. All sampled endpoints are combined by computing a weighted mean. Inverse fit variances are used as weights.

Each set of all these sampled values is used to calculate a value $E_{0,eff}$ according to equation 3.7. By repeated sampling, a distribution of $E_{0,eff}$ values is obtained. Its median value is quoted as the RW tritium final states fit input for the endpoint and its standard deviation as the corresponding one sigma uncertainty.

3.5.4 Patchwise Rear Wall Normalizations

3.5.4.1 Central Values

Since RW count rates of individual patches are very low near the endpoint, it is not simply possible to fit a separate endpoint for each patch. The fit of a normalization in contrast is more robust, as it is sensitive to counts from the entire range of retarding voltages. Therefore only normalization values are determined patchwise.
The tritium final states fit procedure for the patchwise normalizations is in large parts analogous to section 3.5.3. In the following procedure *patches* can be substituted by other groupings of pixels if needed.

RW activity The same RW activity model $A(intflow)$ as for the endpoint analysis (see above) should be used.

RW normalization RW scans are fitted with patchwise normalizations, as well as a common endpoint. The fitted normalizations for each patch are used to calculate a separate factor of proportionality s_p for each patch p.

As the runtime of a measurement run is proportional to the number of RW counts detected in the FPD for a given RW activity, a weighted mean of the estimated RW normalization, taking the runtime of the ith run T_i as weight, is appropriate.

It corresponds to a weighting by the number of RW counts. The normalization for each patch N_p is

$$N_p = \frac{\sum_i s_p A(intflow_i) w_i}{\sum_i w_i}. \tag{3.8}$$

$$w_i = T_i \tag{3.9}$$

This then has to be scaled with equation 3.10.

3.5.4.2 Error Propagation

To compute the uncertainty on the patchwise RW normalizations N_p a MC-Propagation technique, similar to the procedure for $E_{0,eff}$, is used. This means sampling all needed values according to their uncertainties and using these to compute N_p via equation 3.8.
Only the uncertainties of the following models are taken into account.

Uncertainty of the RW activity model Parameters for $A(intflow)$ are sampled similar as in the endpoint analysis propagation procedure described above.

Patchwise RW normalization model The normalization model for the patchwise normalizations is similar to the normalization model for the endpoint analysis above, but treating values for each patch separately.

With equation 3.8 each set of samples values results in a value N_p for each patch p. By repeated sampling a distribution of values for N_p is obtained for each patch. Its median value is quoted as the systematic input and its standard deviation as the corresponding one sigma uncertainty.
To scale these values obtained with an arbitrarily chosen column density $(\rho d)_{fit}$ and tritium purity ϵ_{fit} (see section 3.5.1) to the physical column density $(\rho d)_{KnmX}$ and ϵ_{KnmX} in the neutrino mass analysis (KnmX), they are multiplied with a factor

$$n_p = N_p \cdot \frac{(\rho d)_{fit} \cdot \epsilon_{fit}}{(\rho d)_{KnmX} \cdot \epsilon_{KnmX}}. \tag{3.10}$$

$(\rho d)_{KnmX} \cdot \epsilon_{KnmX}$ is computed as the product of weighted means of the runwise column densities (ρd) and tritium purity values ϵ_i, weighted by the respective runtime T_i of the i$^{\text{th}}$ beta scan. It is not calculated as the weighted mean of the product to replicate the settings of the neutrino mass analysis.

$$(\rho d)_{KnmX} \cdot \epsilon_{KnmX} = \frac{\sum_i (\rho d)_i T_i \sum_i \epsilon_i T_i}{(\sum_i T_i)^2} \tag{3.11}$$

3.6 Tritium Final States Fit Results

The tritium final states fit results were obtained using the method described in section 3.5. Since measurement settings, as well as the available data, differed between measurement campaigns, this sections covers the details of the analysis.
RW scans taken at identical integral flow values were grouped to be analyzed in a combined manner, summing over all counts and corresponding measurement times. Retarding energy values were shifted to the same RW voltage before combination. An overview chart of measurement configurations for RW scans is given in table A.1.

3.6.1 Rear Wall Endpoint Evolution

For each of these combined RW scans a uniform fit (i.e. combining all pixels) was done. Results for the RW endpoints are summarized in figure 3.4. The endpoints seem consistent before the RW cleaning, but weak indications of a trend are seen after the cleaning. This is probably also related to a drift of the RW work function observed at the beginning of the Knm5 campaign, which was compensated with multiple adjustments of the RW voltage (see figure 3.3).
Figure B.1 shows the evolution for the uniform RW normalization and figure B.2 the evolution for the flat background rate.

3.6.2 KATRIN Neutrino Mass 3 & 4

The campaign here denoted as Knm4 does not contain the last runs of Knm4 (Knm4e in figure 3.1), as these are analyzed in combination with Knm5 in the RW analysis (see section 3.6.3) similar to the neutrino mass analysis.

3.6.2.1 Rear Wall Endpoint

One common RW endpoint value for Knm3 and Knm4 was obtained from uniform fits. Since no significant change of the RW endpoint was observed before the RW cleaning, the endpoint fit results of RW scans after Knm3 and after Knm4, but before the first RW cleaning, were combined to obtain a common endpoint. It was calculated as the weighted mean of the three endpoints. The weights were the inverse variances from these fits.
Three distinct effective values for the RW voltage U_{RW} were calculated for campaigns Knm3a, Knm3b and Knm4 (see figure 3.3). Since the effective RW voltage was approximated as constant throughout the three campaigns respectively, the computation of the weighted mean in equation 3.7 reduced to a multiplication with a single factor.
Therefore three distinct effective RW endpoint values result from shifting by the RW voltage (equation 3.5). These results are given in table 3.1.

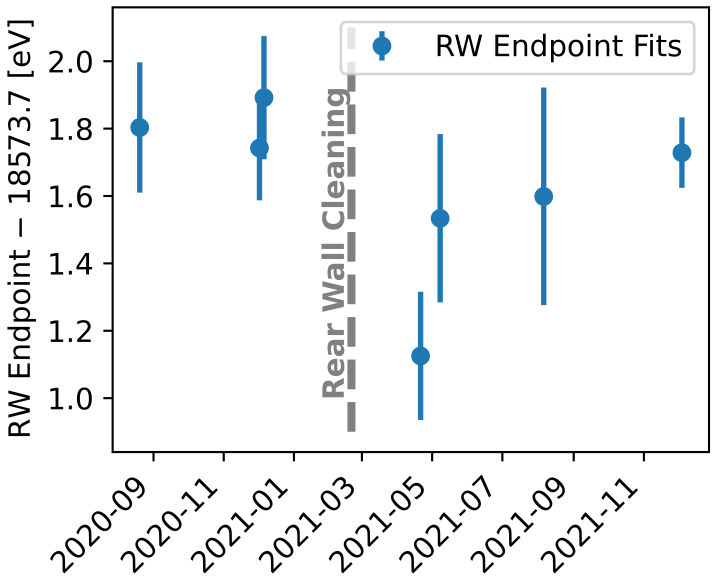

Figure 3.4: Fitted rear wall endpoint results for uniform T_2 spectrum fits at different points in time.

	$E_{0,RW}(U_{RW}=0)$	U_{RW}	$E_{0,RW}(U_{RW})$
Knm3a	18 575.37(10) eV	0.175 V	18 575.20(10) eV
Knm3b	18 575.37(10) eV	0.177 V	18 575.19(10) eV
Knm4	18 575.37(10) eV	0.090 V	18 575.28(10) eV

Table 3.1: Rear wall endpoints for Knm3a, Knm3b and Knm4 before and after shifting by the effective value of the RW voltage set during the respective campaign.

3.6.2.2 Rear Wall Normalization

The Knm3 measurement campaign consisted of two blocks (Knm3a and Knm3b) of distinct experimental conditions for the magnetic fields of the MAC-E filter.

Knm3b Knm3b was measured in a symmetric configuration of the MAC-E filter B-fields (6.3 G setting). The only RW scan in the 6.3 G setting was measured after Knm3, therefore only this one scan was used for the determination of the RW normalization for Knm3b. As the Knm3b neutrino mass analysis is carried out in a uniform manner, only a uniform RW normalization was provided. Equation 3.8 reduced to a multiplicative factor, the uncertainty was calculated by Gaussian error propagation. An estimation of the scaling factor from the RW activity at the time of the 6.3 G RW scan after Knm3 to the effective RW activity during Knm3b was provided by Max Aker and is given in table D.3. With the correction factor (table D.2) scaling to the physical column density and tritium purity according to equation 3.10 the final result is

$$n_{3b} = 0.005\,86(5). \tag{3.12}$$

For comparison, the normalization value for a WGTS spectrum is about 1.18, the RW spectrum comprising less than 1 % of the counts in the FPD.

Knm3a and Knm4 Knm3a and Knm4 were measured in the SAP configuration (see section 2.3) and require patchwise RW normalization inputs.
All RW scans measured after Knm4 were also measured in the SAP setting. These SAP RW scans measured before the RW cleaning were used to determine the patchwise normalizations for Knm3a and Knm4 separately.
Equation 3.8 reduced in complexity to a multiplication with a distinct factor s_p for each patch. The ratios of s_p were taken from patchwise RW normalization fits of RW scans. A factor scaling from the RW activity at the time of the RW scans to the effective RW activity during the neutrino mass campaigns (table D.3) was used. Correlations between patchwise RW normalizations were neglected as the additional m_ν^2 uncertainty induced by the correlations was negligible compared to the impact of the RW endpoint uncertainty. The propagation of uncertainties was done via Gaussian error propagation.
The result was scaled to the correct column density and tritium purity according to equation 3.10 with the values in table D.2. The results are given in table 3.2.

3.6.3 KATRIN Neutrino Mass 5

The data measured in the KATRIN neutrino mass 5 campaign, abbreviated as Knm5, is analyzed in combination with the last part of Knm4 (called Knm4e in figure 3.1).

	Patch number	Normalization
KNM3a	0	0.011 66(16)
	1	0.011 70(16)
	2	0.011 05(15)
	3	0.011 04(15)
	4	0.010 67(14)
	5	0.010 08(14)
	6	0.009 60(13)
	7	0.009 18(12)
	8	0.008 70(12)
	9	0.008 34(11)
	10	0.007 25(10)
	11	0.007 09(10)
	12	0.006 55(9)
	13	0.006 11(8)
KNM3b	uniform	0.005 86(5)
KNM4	0	0.012 80(7)
	1	0.012 84(7)
	2	0.012 13(6)
	3	0.012 11(6)
	4	0.011 71(6)
	5	0.011 07(6)
	6	0.010 54(6)
	7	0.010 08(6)
	8	0.009 55(5)
	9	0.009 15(5)
	10	0.007 96(5)
	11	0.007 78(5)
	12	0.007 19(4)
	13	0.006 71(4)

Table 3.2: Final neutrino mass analysis rear wall input values for the effective RW normalizations for Knm3a, Knm3b and Knm4.

That is because of the fact that measurement configurations of Knm4e rather resembled Knm5 than Knm4a-d. In particular, starting with Knm4e, the pre-spectrometer was turned off, eliminating a Penning trap between the pre-spectrometer and the main spectrometer.

3.6.3.1 Rear Wall Endpoint

RW activity The RW activity model for the time of the measurements of Knm4e and Knm5 is based on multiple measurements of the RW activity throughout the neutrino mass campaigns. Before Knm5 there was a successful RW cleaning which reduced the activity to almost zero. The RW activity models for Knm4e and Knm5 were treated independently, so two distinct models for Knm4e and Knm5 were needed. The model for Knm4e is linear with parameters m and c.

$$A_{Knm4e}(intflow) = m \cdot intflow + c \tag{3.13}$$

The model for Knm5 is a limited growth function with parameters a, k, x_0 and c.

$$A_{Knm5}(intflow) = a \cdot e^{k \cdot (intflow + x_0)} + c \cdot (intflow + x_0). \tag{3.14}$$

A plot of these models is shown in figure 3.5, the fits of the RW activity models were done by Simon Tirolf. Best fit values are given in table D.1.
For the propagation of uncertainties with the MC-propagation method described above, RW activity curves were sampled independently for Knm4e and Knm5 from the fit's respective covariance matrix.

RW normalization Two factors (s_{4e}, s_5) scaling from the RW activity to the RW normalization were computed separately for Knm4e and Knm5 using the normalization fit result of uniform RW scan fits. For s_{4e} RW scans after Knm4 but before the first RW cleaning were used. For s_5 RW scans between the first and the second RW cleaning were used (see table A.1).
From the intermediate MC-Propagation result for the scaling factors, displayed in figure 3.6, it is evident that factors s_{4e} and s_5 are significantly different. This could not be attributed to a specific cause.

Endpoint model Due to the successful RW cleaning after Knm4, the RW endpoint model was assumed to have two distinct endpoints. One endpoint for Knm4e, and one for Knm5. That was assumed because there are indications that the RW workfunction, and therefore the endpoint, drifted after the RW cleaning (compare figure 3.4). Since earlier campaigns covered above (Knm3a, Knm3b, Knm4a-d) were not interupted by RW cleanings, this differentiation was not necessary for these. $E_{0,eff,4e}(intflow)$ and $E_{0,eff,5}(intflow)$ each were computed as a weighted mean of uniform RW scan fit results of the RW endpoint using RW scans after Knm4, but before the RW cleaning and RW scans between RW cleanings respectively. Weights were the inverse variances of the fitted RW endpoints. Using these, the overall effective endpoint $E_{0,eff}$ was calculated with equation 3.7.
With the MC-propagation method described above, the distribution of the resulting

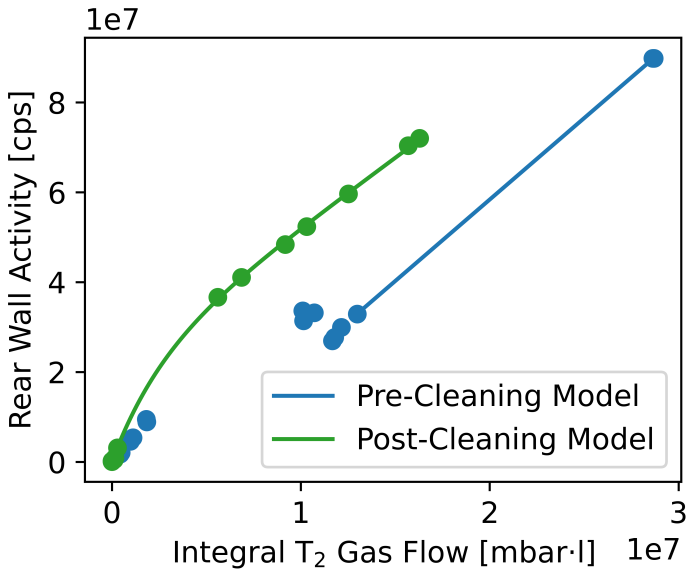

Figure 3.5: RW activity measurements along with RW activity models before (Knm4e) and after (Knm5) the first RW cleaning. The best fit parameters for the shown curves are given in table D.1.

$E_{0,eff}$ values was obtained as shown in figure 3.7. Its median and standard deviation are quoted as tritium final states fit RW final input for the combination of Knm4e and Knm5.

$$E_{0,RW,eff} = 18\,574.95(11)\,\text{eV} \tag{3.15}$$

3.6.3.2 Patchwise Rear Wall Normalizations

Since there are two RW activity models (for Knm4e and for Knm5), also the corresponding patchwise RW normalization fit values were treated independently. Fits used were patchwise RW normalization fits of RW scans after Knm4, but before the RW cleaning, for Knm4e. For Knm5 patchwise RW normalization fits of RW scans between RW cleanings were used. Values for N_p were subsequently calculated according to section 3.5.4.
For calculation of uncertainties, patchwise RW normalizations were sampled for each RW scan fit from its covariance matrix and best fit values. These were scaled to the correct column density and tritium purity according to equation 3.10. The value of the scaling factor is given in table D.2.
The MC-propagation result is one distribution for each of the 14 patchwise RW nor-

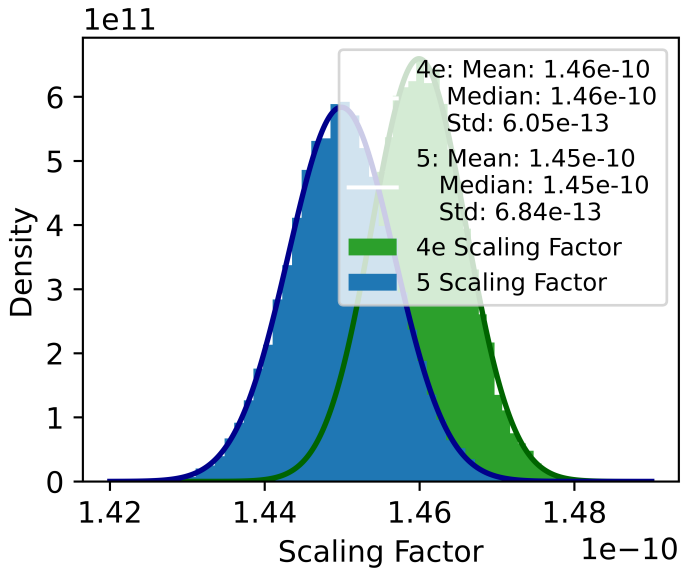

Figure 3.6: Shown are MC-propagation results for the factors s_{4e}, s_5 scaling from RW activity to RW normalization (equation 3.4) for Knm4e and Knm5 separately. Knm4e was before, Knm5 after the first RW cleaning. The RW normalization stems from RW scan fits, the RW activity from measurements at 14 kV retarding voltage with the FBM. The change in value could not be attributed to a specific cause, as in both measurements, as well as the RW cleaning, many factors play a role.

malizations. The median value for each patch, as well as the standard deviation of the corresponding distribution are quoted as final RW input values for the combination of Knm4e and Knm5. Distributions are shown in figure 3.8 and 3.9. The sample correlation matrix for the 14 normalizations is depicted in figure C.1.

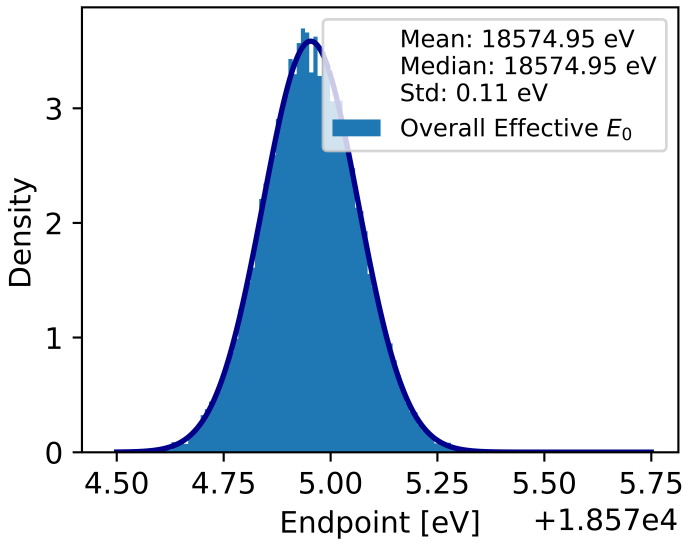

Figure 3.7: MC-propagation result of the effective RW endpoint resulting from the tritium final states fit procedure carried out for the combination of Knm4e and Knm5 described in section 3.6.3. The median and standard deviation are the final RW inputs for the neutrino mass analysis.

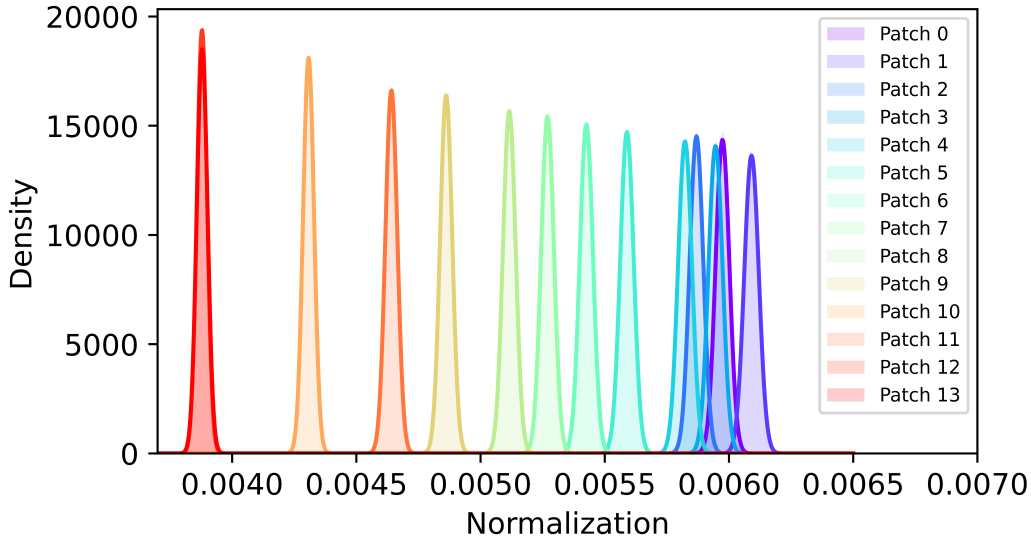

Figure 3.8: Histograms for MC-propagation results of patchwise RW normalizations for the combination of campaigns Knm4e and Knm5. Distributions for patches 12 and 13 are very similar and hard to distinguish in this plot. Patchwise median values and standard deviations are the final RW inputs for the neutrino mass analysis.

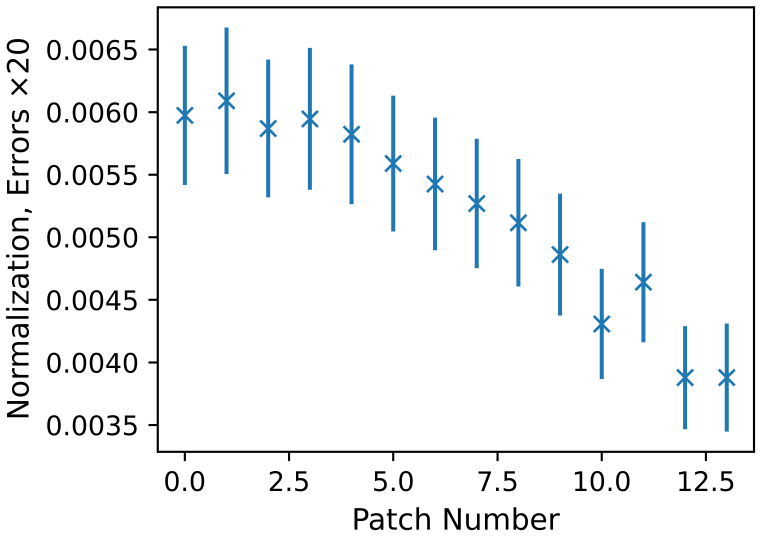

Figure 3.9: Patchwise normalization RW input values for the combined neutrino mass analysis of Knm4e and Knm5. Shown are the median values along with their standard deviations from figure 3.8. The correlation matrix is given in figure C.1.

Chapter 4

Systematics and Neutrino Mass Impact

The tritium final states fit in chapter 3 was done as a baseline description of RW data. The tritium final states fit assumes the RW spectrum to have a shape very similar to a T_2 spectrum, but leaving its endpoint, the signal strength and the rate of a flat background as free fit parameters.
Section 4.1 explores more advanced methods, questioning previous assumptions of the T_2 final states spectrum shape and trying to incorporate the lack of knowledge about the RW spectrum into the analysis. Section 4.2 quantifies said methods' effects on the neutrino mass analysis and compares them in this regard.

4.1 Systematics

4.1.1 Problem Outline

The radioactive material on or inside the RW can not safely be assumed to be T_2. Other molecules come with a different final states distribution when undergoing beta decays and therefore lead to a different integral spectrum. The spectrum should also be altered by the fact that the radioactive molecules cannot be in a gaseous state, unlike inside the WGTS.
As the exact spectrum shape is unknown, statistical treatment of the RW should find a description allowing for a sufficiently large variation of the spectrum. It should also not be overly general, considering scenarios excluded by theory and experimental observations, and consequently overestimating the systematic uncertainty in m_ν^2.
The main problem with this task is the low number of counts measured in the FPD during RW scans. The count rate is usually $< 1\,\%$ compared to the filled WGTS and the measurement time spent on RW scans is very limited. Cumulative runtime spent on RW spectrum measurements is on the order of $2 - 5\,\mathrm{d}$ per neutrino mass campaign. Due to the low number of counts, many fitting methods suffer from the lack of statistical power contained in RW characterization campaigns. As there are no detailed theory predictions, methods that are, to varying degree, based on empirical results have to be employed.

4.1.2 Subtraction Method

The idea behind the *subtraction method* is to directly relate the Poisson uncertainties, that come with counting RW electrons in the FPD, to fluctuations of counts measured during beta scans. The number of counts in a RW scan are taken to be uncorrelated between different retarding voltage settings. One could then try to directly subtract estimations based on measured RW counts from observed WGTS counts at identical retarding energy values.
In the neutrino mass fit this then results in an additional statistical uncertainty on the squared neutrino mass.
Because of problems mentioned below that arise with the use of real RW scan measurement data, this study was done on Asimov data resembling typical RW and WGTS spectra. The generated RW spectrum resembled the best fit outcome of a tritium final states fit of the RW scans done after Knm4 without a flat background. The WGTS spectrum resembled a typical spectrum during the Knm4 campaign. The assumed measurement times were $T_{RW} = 3\,\mathrm{d}$ and $T_{WGTS} = 100\,\mathrm{d}$.
The square root of the Poisson variance for the number of counts $N_{RW}(qU)$ at each value of the retarding voltage U is

$$\sigma_{N_{RW}}(qU) = \sqrt{N_{RW}(qU)}. \tag{4.1}$$

The Poisson error on the RW count rate is shown in figure 4.1. The error on the WGTS counts introduced by subtraction of counts was scaled by the ratio of runtimes

$$\sigma_{N_{WGTS}}(qU) = \sigma_{N_{RW}}(qU) \cdot \frac{T_{WGTS}}{T_{RW}}. \tag{4.2}$$

For determination of the additional statistical uncertainty of the neutrino mass, a MC-propagation method was used. Statistical fluctuations from the RW were sampled from Poisson distributions characterized by $\sigma_{N_{WGTS}}(qU)$ and the difference to the extrapolated RW count rate was added to Asimov WGTS counts. This sampling was repeated, each time subsequently fitting the four WGTS parameters (m_ν^2, E_0, signal normalization, flat background) to the fluctuated spectra in a 40 eV energy fit range.
The resulting distributions for the deviations of best fit values of m_ν^2 and E_0 from the true values are shown in figure 4.2. The additional statistical uncertainty is on the order of $0.02\,\mathrm{eV}^2$ for the simulated scenario. This should be considered a rather optimistic scenario, as not the uncertainties of the unscattered RW scans, but of the estimated scattered integral spectrum were considered.
Furthermore in the described study also the following simplifications were made.

- Flat Background
  In this study the flat background count rate during the RW scans was assumed

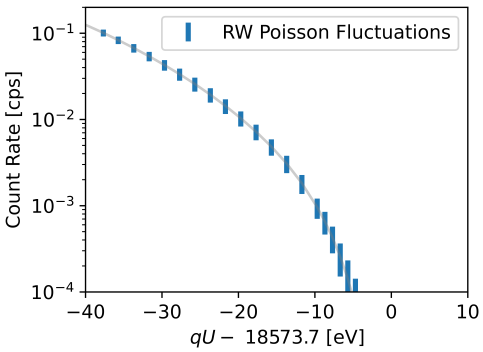

Figure 4.1: Subtraction method: Poisson square root of Poisson variances calculated according to equation 4.1 on RW Asimov integral spectrum data without flat background.

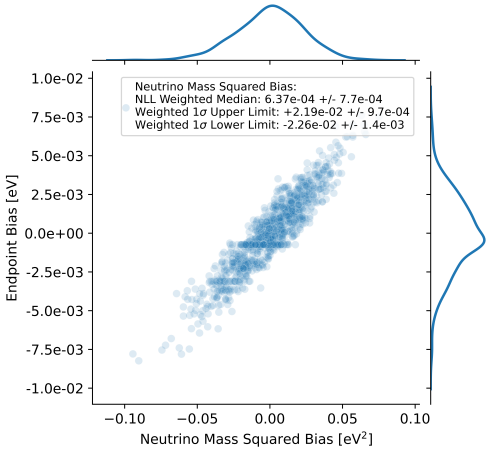

Figure 4.2: Subtraction method: For every qU value, counts were independently sampled from the Poisson fluctuations depicted in figure 4.1, scaled with equation 4.2, and the differences to the central value added to an artificial WGTS spectrum. Shown are the biases of the values of E_0 and m_ν^2 for subsequent fits of the four parameters (signal normalization, flat background, E_0, m_ν^2) with their kernel density estimation.

to be zero, contrary to measured RW data (see figure B.2). To be able to distinguish between the flat background and the RW spectrum in real measurements, the application of some kind of model is required.
This problem could also be easily simplified if the flat background was the same during RW scans and beta scans. That doesn't correspond to observations, as the mean background rate comparing RW scans and beta scans differs significantly ($> 5\,\sigma$) on the order of 10 %.

- Measurement time distribution (MTD)
  The MTD during beta scans was changed multiple times over neutrino mass campaigns up to Knm5. The MTD used for measuring most of the RW scans is a flat MTD (see figure 3.2 for comparison) which is significantly different from the one used for beta scans. The Poisson errors of RW counts can not be propagated to count rates measured at different retarding voltages without

assuming a model for interpolation.

- RW voltage
  The RW voltage (see section 2.6) was changed multiple times during past neutrino mass campaigns to compensate a drift of the optimal RW workfunction (e.g. during the Knm5 campaign, see figure 3.3). This alters the measured count rate at given retarding energy values (see equation 3.5). By setting a specific RW voltage during RW scans, the measurement conditions during beta scans can usually not be exactly replicated.
  Therefore a model is needed to account for differences in RW voltage settings.

In summary, it is clear that one can not solely rely on RW scan data, but some models have to be developed to take the mentioned effects and various measurement settings into account.

4.1.3 Single Final State Distributions

In principle two types of tritium molecules can emerge from the WGTS and reach the RW.
Tritium ions can be magnetically guided along the field lines but are much less likely than electrons to reach the RW, as some are removed by dipole electrodes in the transport section (section 2.2) or are drifting towards the beam tube after scattering.
The second type are neutral T_2 molecules. T_2 molecules are more likely to reach the RW than the main spectrometer, as the pumping sections towards the rear end are shorter and less effective. There are also no chicane sections blocking line-of-sight flight paths from the WGTS to the RW.
After they reach the RW, tritium atoms are presumably bonding with other atoms, forming new radioactive molecules.
From literature final state energies and corresponding transition probabilities for some parent molecules containing tritium atoms are known. These are listed in section 4.1.3.1.

4.1.3.1 Final State Distributions from Literature

In the following, final state distributions (FSDs) are denoted by the parent molecule of the considered beta minus decay.
The FSD used in the neutrino mass analysis for the decay of T_2 (to $^3HeT^+$) was determined by theoretical calculations[25] and experimentally verified recently[26].
Other FSDs, related to tritiated molecules, available from scientific literature, include atomic tritium[27] and a number of hydrocarbons (methane: CH_3T[28][29][30],

ethene: C_2H_3T[30], ethane: C_2H_5T[30], propane: C_3H_7T[31][30]). Furthermore, FSDs of molecules containing nitrogen (ammonia: NH_2T[32], methylamine: NH_2CH_2T[30], ethylamine: $NH_2C_2H_4T$[30]) as well as tritiated water (OHT[32]). For some of these molecules calculations from multiple references were available, yielding significantly different FSDs. The accuracy of these theoretical calculations could not be assessed, but is in many cases assumed to be rather lacking. Estimations of uncertainties for final state energies or transition probabilities were not available and could not be taken into account. In cases where literature provided only binned data, discrete central energy values were estimated. Figures 4.3, 4.4 and E.1 depict said FSDs. General features of a FSD most relevant for the shape of

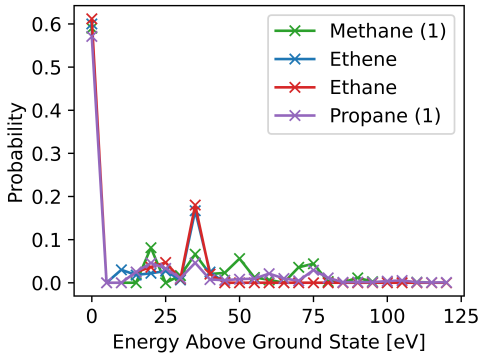

Figure 4.3: Single FSDs: Energies and transition probabilities for various tritiated hydrocarbon final state distributions from literature. Labeled are the parent molecules before the beta decay. States are binned in 5 eV intervals for this plot. Results of different calculations for methane and propane are shown in figure E.1. References: methane (1)[29], ethene[30], ethane[30], propane (1)[31].

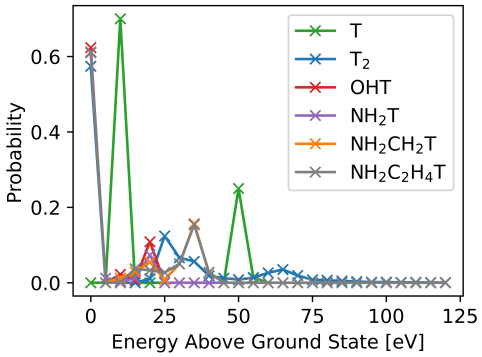

Figure 4.4: Single FSDs: Energies and transition probabilities for considered tritiated non-hydrocarbon final state distributions from literature. Labeled are the parent molecules before the beta decay. States are binned in 5 eV intervals for this plot. References: T[27], T_2[25], OHT[32], NH_2T[32], NH_2CH_2T[30], $NH_2C_2H_4T$[30].

the integral spectrum, are the endpoint, the width and probability of ground states, as well as details of the distribution of excited states. The value of the endpoint is unknown for the FSDs considered. The width of the distribution of ground states is not well known for most of the molecules. Considerable variation concerning the excited states is observed. Kaplan and Smutny[30] describe a $14-20\,\%$ transition probability to an excited states peak at $35-40$ eV excited state energy as a common feature of tritiated organic molecules.

An electron emitted in a transition to a state at a particular energy is unobservable in an integral spectrum for fit ranges not including comparable energy differences to the endpoint. As the RW endpoint was measured to differ on the order of $1 - 2\,\mathrm{eV}$ from the WGTS endpoint (see figure 3.4), counts in the usual KATRIN fit range of $40\,\mathrm{eV}$ are just slightly affected by a feature as described by Smutny and Kaplan.

4.1.3.2 Fits and Neutrino Mass Bias

The question of what would happen if the true RW FSD was *FSD X*, but a different, wrong *FSD Y* was used for the fit of RW data and consequently the neutrino mass analysis, was assessed as follows.

1. A RW scan measurement was generated with a FSD X.
2. A WGTS measurement with a RW FSD X background spectrum was generated.
3. The RW data from step 1 was fitted with FSD Y, determining an endpoint and a signal normalization. The fitted energy range was $120\,\mathrm{eV}$.
4. The WGTS data from step 2 was fitted with the regular four WGTS parameters and a fixed RW background spectrum of FSD Y with the corresponding RW parameters determined in step 3.
5. The resulting best fit value of m_ν^2 was retrieved to assess the impact on the neutrino mass fit.
6. Steps 3 to 5 were repeated with a variety of FSDs Y.

As a true FSD X the T_2 FSD, with RW parameters as determined from fitting RW scans after Knm4, was chosen. A broad variety of FSDs mentioned above were used as FSD Y. Also a FSD with only a single ground state and no excited states (*Disabled*) was included for comparison.
χ^2 values of the fits in step 3 are depicted in figure 4.5. It shows that fitting with different FSDs for most molecules yields a relatively small χ^2, meaning that these can not be clearly differentiated from the T_2 FSD with the given statistics.
The fit in step 4 was repeated for fit ranges $40\,\mathrm{eV}$, $60\,\mathrm{eV}$ and $120\,\mathrm{eV}$. The m_ν^2 biases from step 5 are shown in figure 4.6. Since the FSDs Y mainly differ in the excited states, which become more prominent in the integral spectrum as the absolute value of the retarding potential is decreased, the spread in m_ν^2 values gets larger as the fit range in step 4 is increased.
For the $40\,\mathrm{eV}$ fit range, considering only hydrocarbon FSDs, simulated m_ν^2 biases are $\leq 0.009\,\mathrm{eV}^2$. Hydrocarbons could be a likely candidate for molecules formed on the RW. When interpreting this maximum value for the m_ν^2 bias as uncertainty it would be one of the smallest KATRIN systematics, when compared to the effects considered in the Knm2 analysis[12].

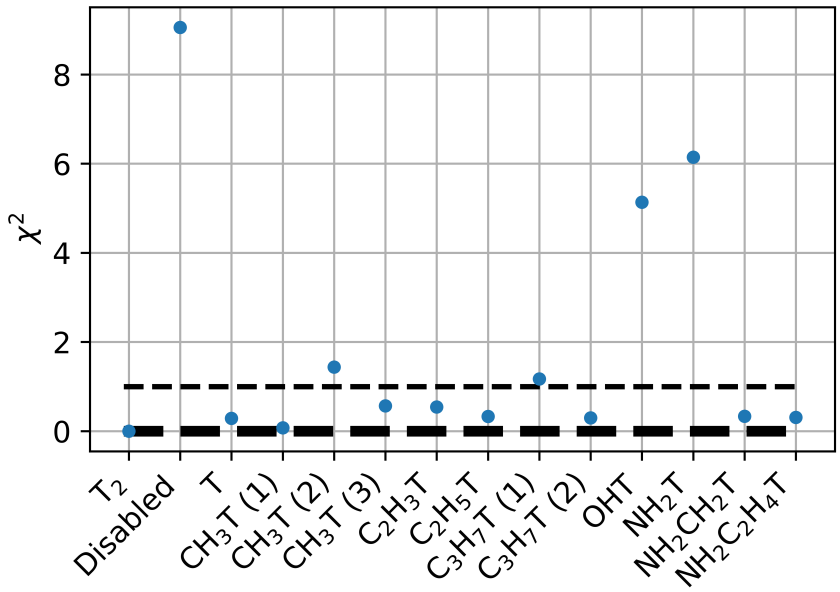

Figure 4.5: Single FSDs: χ^2 values of fits with various FSDs from literature to an Asimov T_2 RW spectrum with a fit range of 120 eV. FSDs for which multiple literature references were considered are: CH_3T (1)[29], CH_3T (2)[28], CH_3T (3)[30], C_3H_7T (1)[31], C_3H_7T (2)[30]. Other FSD references are given in section 4.1.3.1.

4.1.4 FSD-Onset Method

To improve the T_2 spectrum fit to RW data, a new empirical spectral parameter was introduced and fitted as additional free parameter. It is here called the *FSD-Onset* parameter[33].
The idea behind the FSD-Onset parameter F is to modify the ratio of transition to ground and excited states (probabilities P_g and P_e) by introducing a multiplicative scaling factor.

$$\frac{P'_g}{P'_e} = \frac{1+F}{1-F}\frac{P_g}{P_e} \tag{4.3}$$

F is defined on the interval $[-1, 1[$. $F = 0$ corresponds to the unmodified ratio, $F \to 1$ to a zero excited state probability and $F = -1$ to a zero ground state probability. An illustration of this scaling is shown in figure 4.7.
The modified ground and exited states probabilities are obtained to be

$$P'_g(F) = \frac{(1+F)P_g(P_g+P_e)}{(1+F)P_g + (1-F)P_e} \tag{4.4}$$

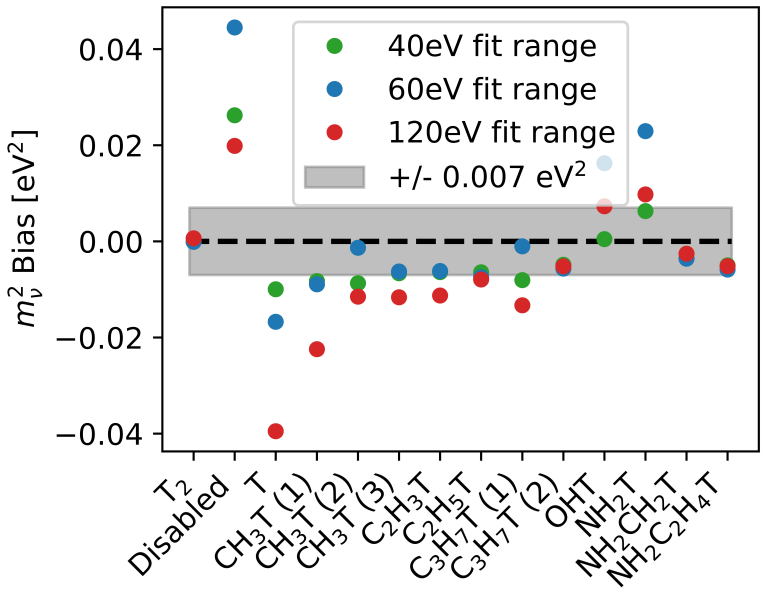

Figure 4.6: Single FSDs: Best fit values of fits with various FSDs from literature to a T_2 Asmiov RW spectrum (χ^2 values in figure 4.5) were used to correct by the same Asimov RW in a neutrino mass fit. Resulting biases of the best fit m_ν^2 are shown. The FSDs for which multiple literature references were considered are: CH_3T (1)[29], CH_3T (2)[28], CH_3T (3)[30], C_3H_7T (1)[31], C_3H_7T (2)[30]. Other FSD references are given in section 4.1.3.1.

$$P'_e(F) = \frac{(1-F)P_e(P_g+P_e)}{(1+F)P_g+(1-F)P_e}. \tag{4.5}$$

Fits of RW data from the first RW scans after Knm4, but before the first RW cleaning, with the FSDs introduced in section 4.1.3 were carried out in a 120 eV energy fit range. Fits were repeated with and without a free FSD-Onset parameter. A comparison of the resulting χ^2 values is shown in figure 4.8.
One can see that the large spread of χ^2 values is greatly reduced by the introduction of the FSD-Onset parameter. The FSD-Onset can therefore be used as a proxy, effectively absorbing the variance between different molecules' FSDs in one parameter.
The RW systematic uncertainty for m_ν^2 is determined by generating a combined WGTS and RW spectrum. This spectrum is then fit with the parameters used for generating, but sampling the RW parameters (RW endpoint, RW normalization, RW FSD-Onset) from the RW fit's covariance matrix and best fit values. Free fit parameters were the usual WGTS variables (m_ν^2, E_0, signal normalization, flat background).

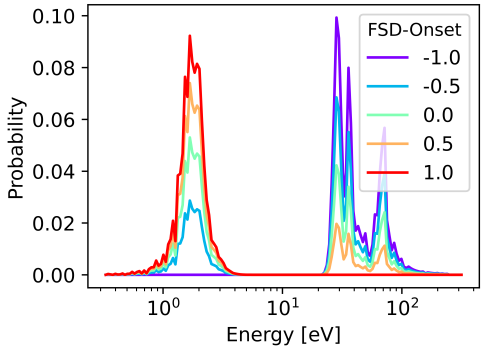

Figure 4.7: FSD-Onset: Effect of a multiplicative scaling factor for the ratio of ground to excited state transition probability. 1 corresponds to zero excited state probability, -1 to zero ground state probability (equation 4.3). Intermediate values represent a smooth interpolation.
Shown is the T_2 final state distribution with binned probabilities and equal spaced energy log scale binning.

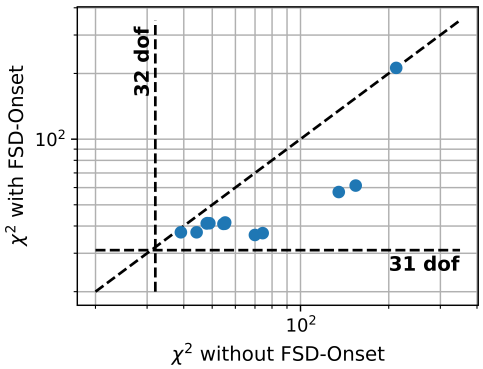

Figure 4.8: FSD-Onset: Comparing χ^2 values of fits of the first RW scan after Knm4 with and without a FSD-Onset as free fit parameter. The points correspond to the final state distributions listed in figure 4.6. The FSD on the diagonal doesn't contain excited states. Degrees of freedom are depicted for each fit.

The width of the distribution of best fit values for m_ν^2 is quoted as RW systematic uncertainty.
With this method the resulting m_ν^2 uncertainty for the Knm4 campaign was calculated to be about $0.002\,\mathrm{eV}^2$ for the neutrino mass fit. Using this value would make the RW one of the smallest systematic effects considered in the neutrino mass analysis[12].

4.1.5 Parameterized Final States Distribution

4.1.5.1 Parameterized FSD Principle

Applied to the neutrino mass analysis, the parameterized FSD approach aims to simplify the computation of the effect of the FSD on the differential spectrum. In the following, the differential spectrum formula for the parameterized FSD approach is derived.

From equation 1.25 the following proportionality relation is approximated

$$\frac{d\Gamma}{dE} \propto \sum_i P_i \epsilon_i \sqrt{\epsilon_i^2 - m_\nu^2}\Theta(\epsilon_i - m_\nu). \tag{4.6}$$

It contains the summation over all excited states with probability P_i and energies V_i (see equation 1.26).
The FSD calculated from theory contains discrete energies V_i. Inside the WGTS there is tritium gas at a temperature of $27 - 30\,\mathrm{K}$. In a gaseous phase thermal motion will cause a Doppler broadening of the final state energies, which corresponds to a convolution of the FSD with a Gaussian kernel. Some other systematic effects can also be described as an effective broadening and combined with the Doppler broadening.
The delta functions of the discrete states are therefore broadened to Gaussian functions. The entire FSD therefore becomes a sum of Gaussians. If the broadening is sufficiently large, the continuous broadened FSD can be approximated with only a small number of Gaussian functions.

$$P(V, \boldsymbol{\mu}, \boldsymbol{\sigma}, \boldsymbol{A}) = \sum_j A_j \cdot \frac{1}{\sqrt{2\pi}\sigma_j} \cdot exp\left(-\frac{(V-\mu_j)^2}{2\sigma_j^2}\right) \tag{4.7}$$

Each Gaussian function is characterized by three parameters. μ_j represents the mean and σ_j^2 the variance of the j^{th} Gaussian. A_j is used to scale the amplitude.
The parameters of equation 4.7 are determined by fitting to a FSD with a specific broadening. For a T_2 FSD at least four Gaussian functions are needed. The fit illustrated in figure 4.9 (0.2 eV broadening) agrees to about 7×10^{-3} in the 40 eV range.
Using this approximation, equation 4.6 can be simplified, if the following Taylor expansion holds.

$$\epsilon_i \sqrt{\epsilon_i^2 - m_\nu^2} \approx \epsilon_i^2 - m_\nu^2/2 \tag{4.8}$$

It is only valid if

$$\epsilon_i^2 = (E_0 - E - V_i)^2 \gg m_\nu^2, \tag{4.9}$$

which in general is not true for energies close to the endpoint. The expansion of equation 4.8 is valid and exact for the RW analysis, as m_ν^2 is always set to zero there. Hence the definition of the Gaussian function approximation (equation 4.7) is inserted into equation 4.6. The summation in equation 4.6 becomes an integral for

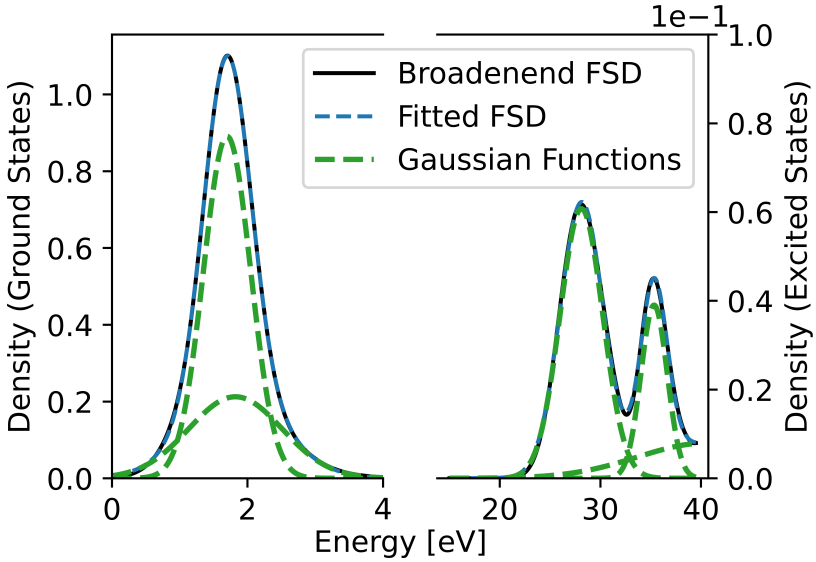

Figure 4.9: Parameterized FSD: A broadened T_2 FSD (0.2 eV broadening) fitted with five Gaussian functions. Two Gaussians were used for the ground state peak and three for the excited states up to 40 eV. The fit agrees up to about 7×10^{-3} in the shown range.

a continuum of final states.

$$\int_{-\infty}^{E_0-E-m_\nu} dV \sum_j \frac{1}{\sqrt{2\pi}\sigma_j} e^{-\frac{(V-\mu_j)^2}{2\sigma_j^2}} \left((E_0-E-V)^2 - \frac{m_\nu^2}{2}\right) =$$
$$\sum_i A_j \left(\frac{1}{2} Erfc\left(-\frac{E_0-E-m_\nu-\mu_j}{\sqrt{2}\sigma_j}\right) \cdot \left[\sigma_j^2 + (E_0-\mu_j-E)^2 - \frac{m_\nu^2}{2}\right]\right.$$
$$\left. + \frac{\sigma_j}{\sqrt{2\pi}}(E_0-E-\mu_j+m_\nu) e^{-\frac{(E_0-E-m_\nu-\mu_j)^2}{2\sigma_j^2}}\right). \quad (4.10)$$

4.1.5.2 Application to the Rear Wall Problem

For the application of the parameterized FSD concept to the investigation of the RW spectrum, the goal is to obtain a description of the differential RW spectrum with few parameters. The approximation method in section 4.1.5.1 is used to reduce the

description of the differential spectrum shape in complexity.
The exact shape of the RW spectrum is uncertain, but it is assumed to contain ground states and excited states. The details of the RW final state distribution's description are determined with a fit.

4.1.5.3 Fitting and Results

A fit using a parameterized FSD model is carried out by first computing the differential spectrum (equation 4.6) for a set of Gaussian parameters containing a fixed number of Gaussians. The integral spectrum is then calculated via equation 2.14. This integral spectrum is compared to fit data and Gaussian parameters are subsequently varied to find values compatible with the data.
Unlike in a fit of the T_2 FSD (figure 4.9), a description consisting of only two Gaussian functions was chosen for fitting the RW scan data measured after Knm4, but before the first RW cleaning, in a 120 eV fit range. Although the data used has the highest statistics of all RW scans up to Knm6, it lacks the statistical power to reasonably fit more than two Gaussian functions.
In addition to the two sets of parameters (μ_1, σ_1^2, A_1, μ_2, σ_2^2, A_2) a flat background rate was left as a free fit parameter. For this fit the endpoint was fixed to 18 575 eV, values of μ_1 and μ_2 are given relative to this endpoint.
In the presented study a gradient based No-U-Turn-Sampler Markov-Chain-Monte-Carlo (NUTS-MCMC[34]) approach was utilized for fitting. Chosen priors were very broad Gaussian functions excluding unphysical values < 0 for σ^2 and A.
The samples drawn with the MCMC were subsequently evaluated using the parameters' posterior distributions after convergence.
The resulting posteriors are shown in figure 4.10. The fitted two Gaussian functions can be interpreted as a narrow Gaussian close to the endpoint representing ground state energies and a very broad Gaussian far from the endpoint describing all excited states. As the RW scans are not very informative due to low statistics, the resulting posteriors for the second Gaussian were still rather broad.
The posterior of μ_2 peaks at a high value of about 80 eV suggesting that the fitted second Gaussian, corresponding to excited state energies, doesn't contribute much to transition probabilities in the usual 40 eV fit range of the neutrino mass analysis. Calculating the cumulative probability in the 40 eV range and comparing it to the total transition probability to either ground state or excited states, yields figure 4.11. One can see that more than 90 % of the Gaussian closer to the endpoint is contained in the 40 eV interval, but the second Gaussian lies mostly outside this range. The ratio of the probability contributed by the second Gaussian in the 40 eV range is shown in figure 4.12. It always contributes less than 15 %, 50 % of all samples show less than 1 % contribution. This indicates that the integral spectrum in the 40 eV range is very much dominated by ground states.

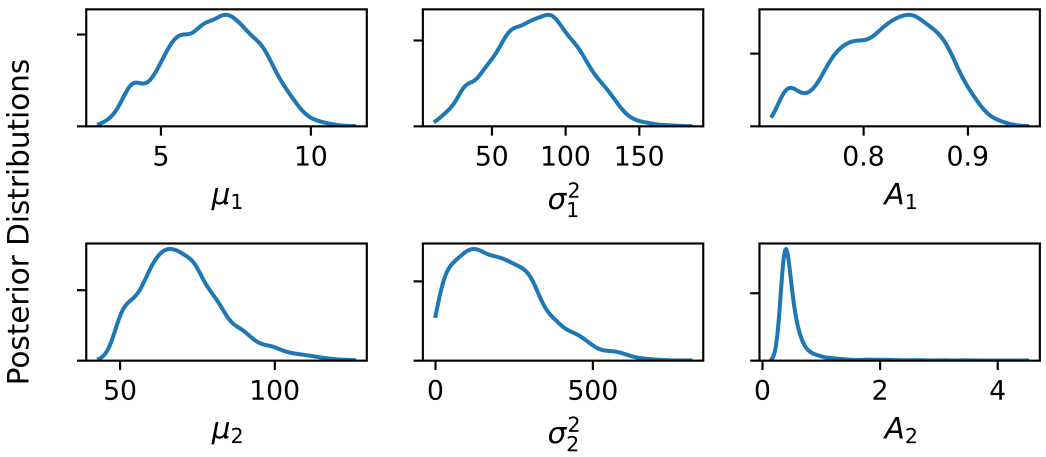

Figure 4.10: Parameterized FSD: Posterior distributions for a two Gaussian parameterized FSD MCMC fit of RW data. The Gaussians are each characterized by a mean (μ), a variance σ^2 and an amplitude A. The posterior distribution for the flat background rate is not shown.

Normalized residuals of posterior predictive distributions for all MCMC samples, as well as a tritium final states fit (section 3.5) with and without FSD-Onset (section 4.1.4) are shown in figure 4.13.
The systematic uncertainty introduced into the neutrino mass analysis based on the MCMC fit results was evaluated.
The samples values are significantly correlated for some fit parameters. Pairplots are given in figures F.2 and F.1. For propagation the sample covariance matrix for the MCMC samples was calculated. This approximation yielded to first order similar results to repeatedly drawing, from the number of MCMC samples, a single random sample, and using its parameters in the neutrino mass fit.
As there is no clearly defined central value or best fit for the results of this analysis, a few options were investigated. Central values could e.g. be defined by point estimates of the parameters' posterior distributions. This is essentially neglecting all correlations between parameters values for the central value estimation. Figure 4.14 shows the residuals when taking the mean, median or mode of each posterior distribution. The choice between these three options doesn't make a significant difference in m_ν^2 for the neutrino mass analysis in the 40 eV range.
The systematic uncertainty on m_ν^2, associated with this fit, was determined by generating a combined WGTS and RW Asimov spectrum and fitting with RW parameters repeatedly sampled from distributions characterized by central values and the ob-

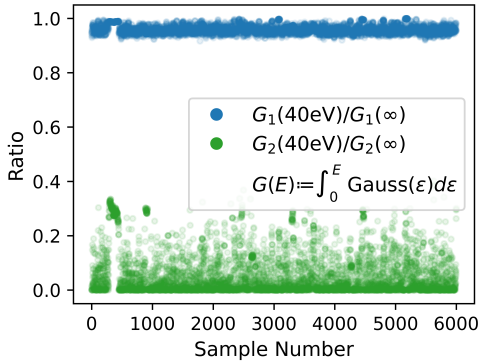

Figure 4.11: Parameterized FSD: Samples from a MCMC fit with two Gaussian functions to RW data as described in section 4.1.5. Depicted is the ratio of cumulative probability densities in the 40 eV range to the total probability for each Gaussian.

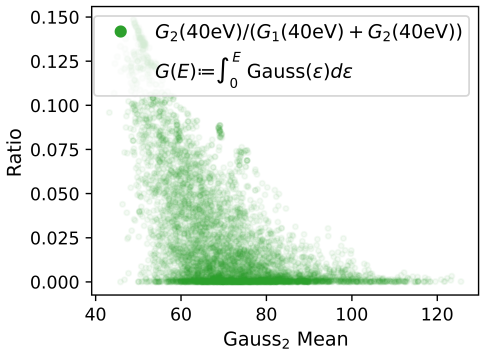

Figure 4.12: Parameterized FSD: Results of a MCMC parameterized FSD fit with two Gaussians to RW data (section 4.1.5). Shown is the mean of the Gaussian function corresponding to excited states, compared to the ratio of probability density from this Gaussian in the 40 eV range to the total cumulative probability in the 40 eV range.

tained sample covariance matrix mentioned above. Free fit parameters were the usual WGTS parameters (m_ν^2, E_0, signal normalization, flat background). The m_ν^2 best fit values are shown in figure 4.15. Its negative-log-likelihood weighted 1σ-tails were used to compute a systematic uncertainty value of $0.05\,\text{eV}^2$.
At this uncertainty value it would contribute one of the largest systematic uncertainties in KATRIN.

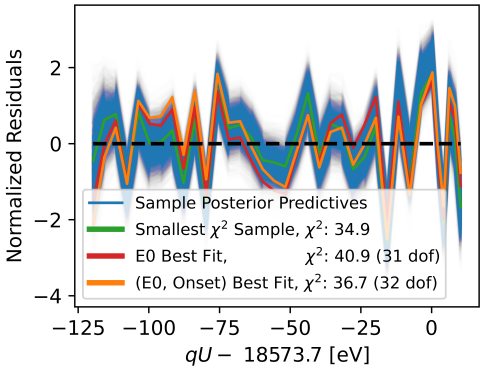

Figure 4.13: Parameterized FSD: In blue are the residuals of posterior predictives for all MCMC samples in the parameterized FSD fit. Highlighted is the MCMC sample with the smallest χ^2 value. Residuals of independent tritium final states fits with and without free FSD-Onset parameter are shown for comparison.

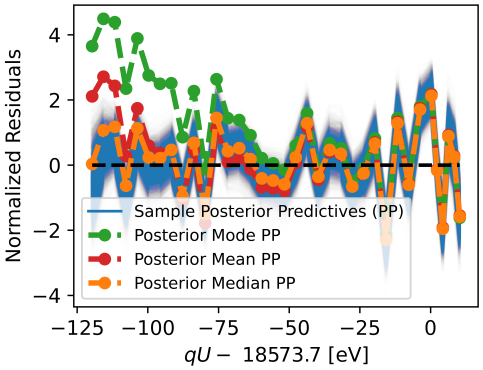

Figure 4.14: Parameterized FSD: In blue are the residuals of posterior predictives for all MCMC samples in the parameterized FSD fit (identical to 4.13). Posterior predictives for different point estimates of central values from the posterior distributions (see figure 4.10) are depicted for comparison.

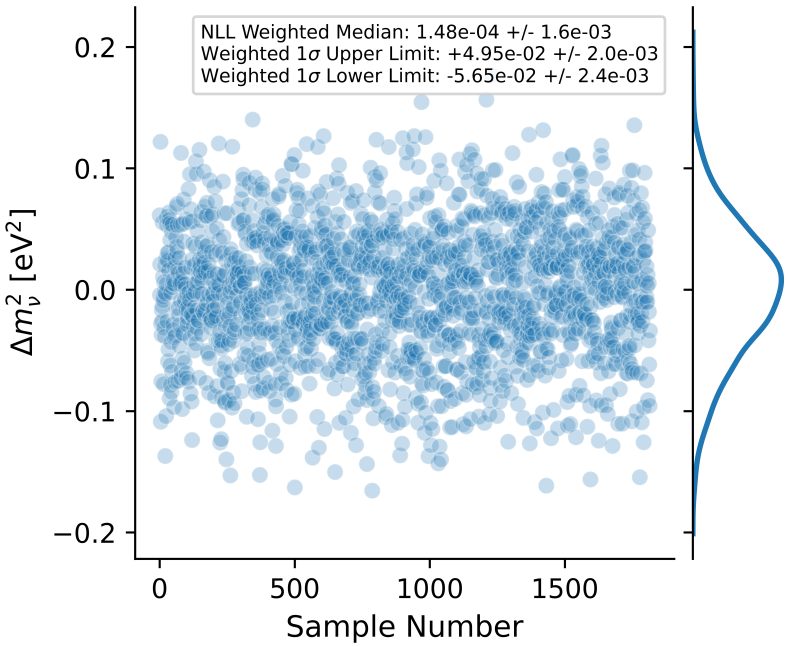

Figure 4.15: Parameterized FSD: Distribution of m_ν^2 bias values in the neutrino mass analysis when sampling RW parameters according to the approximated covariance matrix and mean point estimates of the posteriors from the MCMC.

4.1.6 Combination Method

The molecules comprising the contamination of the RW are unknown. To generalize the approach of fitting a single molecule spectrum (section 4.1.3), the uncertainty introduced by assuming a combination of spectra was explored.
A WGTS spectrum at KATRIN final statistics with an additional RW spectrum at the measured RW activity level after Knm4, was generated. The RW spectrum consisted of a sum of three RW spectra (CH_3T[30], C_2H_3T[30], C_3H_7T[30]) in equal parts. Since, for the RW spectra chosen for combination, the endpoint energies were unknown, these were all shifted to the same ground state energy. In a uniform 40 eV fit range fit of the combined data, the WGTS parameters (m_ν^2, E_0, signal normalization, flat background) as well as a RW endpoint and molecule ratios for the same three molecule species were fitted. The sum of ratios was constrained to 1.000(13) with a pull term. The individual ratios were included with a very broad Gaussian pull term at 0.33(100).
As the differences between the three spectra are very small and the spectrum is dominated by the WGTS, the variation in terms of χ^2 values was too small to accurately recover the true ratios. A profile likelihood scan for m_ν^2 was done to obtain the additional statistical uncertainty caused by the introduction of these nuisance parameters. The additional uncertainty was about $2.8 \times 10^{-3}\,\mathrm{eV}^2$. To account for the entire RW uncertainty this value should be combined with an uncertainty from a fit of the RW normalization. So its total uncertainty is estimated to be about $3 \times 10^{-3}\,\mathrm{eV}^2$, which would still be one of the smallest systematic effects considered in KATRIN.

4.2 Impact on Neutrino Mass Determination

4.2.1 Comparison of Rear Wall Analyses

As a baseline fit the RW analysis assuming tritium final states is certainly underestimating the determined RW systematic uncertainty of $0.001\,\mathrm{eV}^2$. The molecules on or inside the RW can not be assumed to be T_2, because in the present RW setup these are not expected to be able to stick to the RW without bonding.
The subtraction method could be thought to require relatively few assumptions by considering Poisson fluctuations of measured RW counts, but due to the variation of measurement settings during the neutrino mass campaigns, as well as differences to the RW characterization configuration, it also has to employ a model for interpolation of the integral spectrum. The uncertainty of $0.02\,\mathrm{eV}^2$ quoted above, while being relatively large compared to other KATRIN systematics, was obtained not considering scattering in the WGTS, and is therefore most likely underestimating its true value.

The single FSD approach resulted in a maximum neutrino mass squared bias of about $0.009\,\mathrm{eV}^2$ for hydrocarbons, compared to a T_2 spectrum. This is much larger than uncertainties assuming tritium final state distribution, resulting in a significant contribution to the KATRIN total systematic budget of $0.017\,\mathrm{eV}^2$[13]. The main problem with this analysis is the availability of FSDs. The range of molecules for which reference calculations are published is very small. No references are found for tritiated long-chain hydrocarbon beta decays, but these are thought to likely also contribute to the RW activity. The choice of which FSDs to include in the analysis is very difficult, as the true RW contamination is unknown and molecules can not confidently be excluded by fitting to RW data.
The extension of the free fit parameters by the FSD-Onset can greatly reduce the effect of the variations between different FSDs while just leading to a small RW uncertainty of about $0.002\,\mathrm{eV}^2$. If one is accepting the use of empirical parameters, it could be an effective proxy variable for fitting RW data.
The parameterized FSD approach has the problem, that low statistics makes it difficult to extract information, about as many as at least 7 fit parameters, from RW data. With this large number of parameters the uncertainties become very large. Although large parts of the fitted spectrum do not lie in the range of interest used for the neutrino mass analysis, the induced m_ν^2 uncertainty is still very large at $0.05\,\mathrm{eV}^2$. To treat fractions of RW contributions from different molecules as nuisance parameters leads to an additional statistical uncertainty of about $0.003\,\mathrm{eV}^2$ on KATRIN final statistics. Though, the assumptions of a known set of molecules, comprising the RW contamination, could be problematic. If e.g. long-chain hydrocarbons would be found to exhibit great variation in their spectra, the choice of molecule species as well as the number of species would become relevant.

4.2.2 Rear Wall Analysis Methods Breakdown

The RW descriptions presented in sections 3.6 and 4.1 all result in different values for the corresponding uncertainty of m_ν^2. A comparison is shown in figure 4.16. The goal of $0.0075\,\mathrm{eV}^2$ is set in the KATRIN design report[13] for five individual systematics, not mentioning the RW. However, other systematics, as e.g. the high voltage system mentioned, will not contribute significantly to the total systematic uncertainty. The goal for the total systematic uncertainty budged is $0.017\,\mathrm{eV}^2$.

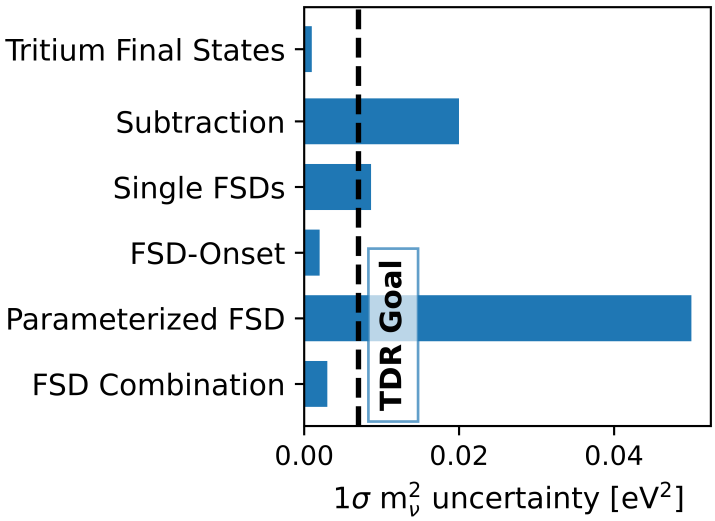

Figure 4.16: Comparison of methods for describing the KATRIN rear wall focused on in this thesis. The dotted line shows the KATRIN technical design report[13] goal set for five individual systematics ($0.0075\,\mathrm{eV}^2$). The report doesn't include any RW uncertainty, but other effects mentioned, e.g. the high voltage system, will not significantly contribute to the KATRIN final total systematic uncertainty.

Chapter 5

Conclusion and Outlook

In this thesis the task of correcting the KATRIN neutrino mass data for the time-dependent background spectrum emerging from a radioactively contaminated part of the experimental setup was undertaken.
The complexity of the treatment of this beta decay spectrum, stemming from the rear wall (RW), lies in the dependency of the spectrum on the history of tritium circulation inside in the KATRIN beam tube, and the very limited knowledge of the physical processes involved. A priori its description is unclear, and measurement time dedicated to RW background characterization scarce.
The task of the analysis comprised developing a description of the influence of the RW, use it to correct the KATRIN spectrum, and estimate uncertainties accordingly.
The first model taken as a baseline description of the spectrum was a modified tritium beta decay spectrum. As tritium molecules are not the source of the spectrum, this fit is not entirely correct and is most certainly underestimating uncertainties, which for this analysis were on the order of $0.001\,\mathrm{eV}^2$.
A further description explored, was the application of spectra calculated for other tritiated molecules, such as short-chained hydrocarbons and a number of short molecules containing nitrogen atoms. These can not be excluded as source of the RW spectrum a priori. Statistical power of the measured data didn't allow conclusive inferences, but simulated m_ν^2 values in the neutrino mass analysis were only shifted by about $0.009\,\mathrm{eV}^2$ depending on the choice within a reasonable set of hydrocarbon molecules.
The additional introduction of an empirical spectral parameter was shown to be able to absorb most of the variance between a wide range of tritiated molecules' spectra known from literature. Using this unphysical proxy variable, the RW systematic uncertainty was still found to be small.
Assuming a mixture of molecules and treating ratios as nuisance parameters did only result in an additional systematic uncertainty of about $0.003\,\mathrm{eV}^2$ on KATRIN final statistics.
Imposing only minimal requirements on the shape of the RW final state distribution and determining its features with a fit using the parameterized FSD method, lead to a description which could not be directly related to a physical system and also

yielded very large uncertainties on m_ν^2.
It was pointed out that avoiding a model of RW final states entirely, still requires a model or some type of interpolation to account for variations of measurement setting during the neutrino mass campaigns and also leads to considerable uncertainties of the neutrino mass result.
The KATRIN collaboration could not decide on a specific approach for the neutrino mass analysis, especially for larger fit ranges as the theoretical knowledge of current FSDs is limited. Efforts of computing FSDs for a broader range of tritiated hydrocarbons are currently pursued at KIT. When energy fit ranges are going to be enlarged beyond 40 eV in the future, these further theoretical calculations paired with the FSD combination approach could be a promising option. Also a refinement of the subtraction method incorporating both Poisson fluctuations and a tritium beta decay spectrum is being investigated.
However, this work has shown that the impact of different RW spectra is small in the 40 eV range for Knm3 to Knm5. Therefore, the tritium final states approach along with a statement on possible systematics is recommended for this data release.

A Rear Wall Measurement Configurations

RW Dataset	MTD	B-field	RW Voltage [V]	Est. Intflow [mbar·l]	Runs	# Runs
after Knm3	flat	6.3 G	0	16558096	64112-64134 46277-64294	41
after Knm4	flat	SAP	0.09	28636315	66337-66361	25
after Knm4	flat	SAP	0	28704651	67015-67032	18
1st RW cleaning						
1st break Knm5	flat	SAP	0.3	5630073	68271-68272	2
1st break Knm5	flat	SAP	0	5630073	68274-68283 68287-68319	43
1st break Knm5	flat	SAP	0.3	5630073	68284-68285 68321-68322 68328-68329 68466-68467 68505	9
2st break Knm5	Knm5	SAP	0	6853287	68662-68666	5
2st break Knm5	flat	SAP	0	6853287	68680-68695	16
2st break Knm5	Knm5	SAP	0	6853287	68696-68704	9
2nd RW cleaning						
before Knm6	flat	SAP	0	15685681	69840-69847	8
after Knm6	flat	SAP	0	28406663	71192-71239	48

Table A.1: Overview of all RW scan configurations until the end of Knm6.

B Rear Wall Time Evolution

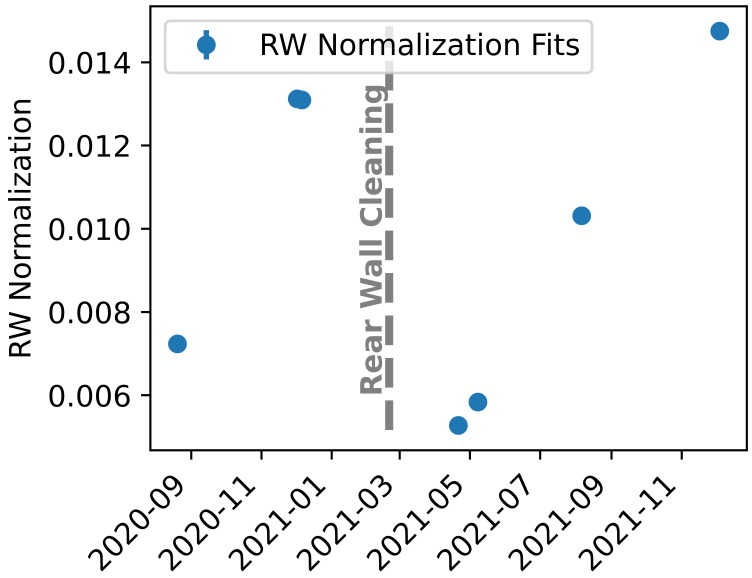

Figure B.1: Rear wall normalization values for uniform T_2 spectrum fits of different RW scans measured at different points in time.

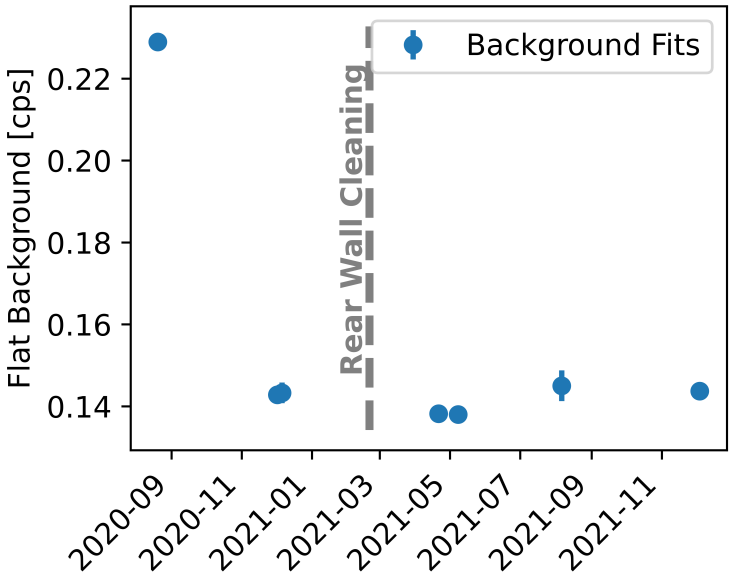

Figure B.2: Rear wall background rate for uniform T_2 spectrum fits of different RW scans measured at different points in time.

C KATRIN Neutrino Mass 5 Patchwise Rear Wall Normalizations

Patch Nr.	Normalization	Standard Deviation
0	0.005 974	2.8×10^{-5}
1	0.006 091	2.9×10^{-5}
2	0.005 869	2.7×10^{-5}
3	0.005 946	2.8×10^{-5}
4	0.005 823	2.8×10^{-5}
5	0.005 589	2.7×10^{-5}
6	0.005 426	2.6×10^{-5}
7	0.005 270	2.6×10^{-5}
8	0.005 116	2.5×10^{-5}
9	0.004 862	2.4×10^{-5}
10	0.004 308	2.2×10^{-5}
11	0.004 641	2.4×10^{-5}
12	0.003 879	2.1×10^{-5}
13	0.003 879	2.2×10^{-5}

Table C.1: Final patchwise normalization input values n_p for the tritium final states fit of Knm4e and Knm5 combined.

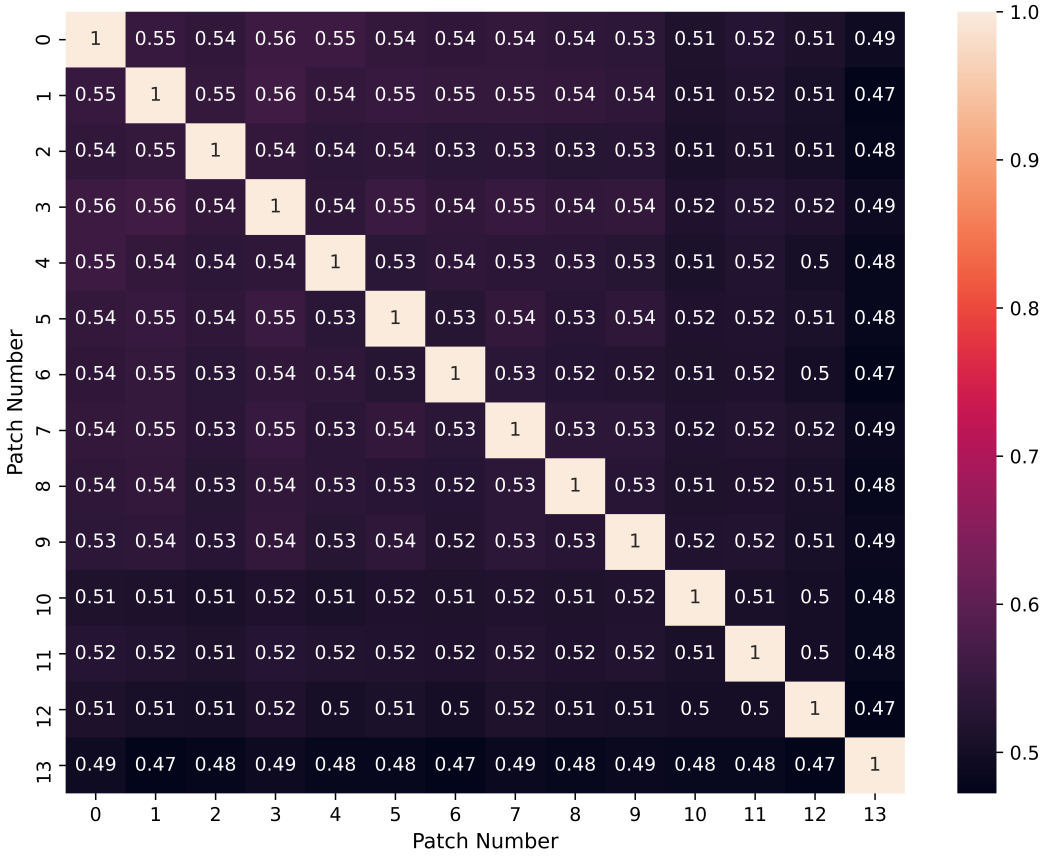

Figure C.1: Correlation matrix of results for the patchwise normalizations n_p for the combination of Knm4e and Knm5.

D Rear Wall Scaling Factors

Campaign	**Parameter**	**Best fit value**
Knm4e	m	3.624 468 620 476 408
	c	−14 118 658.116 692 113
Knm5	a	−296 157 576.699 074 4
	k	$-3.840\,908\,001\,105\,831\,5 \times 10^{-7}$
	x_0	6 865 566.793 789 566 5
	c	3.097 589 868 064 652 3

Table D.1: Best fit parameters of the RW activity models for Knm4e and Knm5 (equations 3.13 and 3.14). Fits were done by Simon Tirolf.

Campaign	ρd	ϵ	$\rho d \cdot \epsilon$ [m^{-2}]	Scaling Factor
RW Scan Fit Reference	3.75×10^{21}	0.98	3.675	1
KNM3a	$2.080\,904\,89 \times 10^{21}$	0.984 722 108	$2.049\,153\,98 \times 10^{21}$	1.793 423 059
KNM3b	$3.750\,438\,7 \times 10^{21}$	0.982 607 436	$3.685\,271\,97 \times 10^{21}$	0.997 212 696 9
KNM4a-d	$3.767\,306\,03 \times 10^{21}$	0.983 644 029	$3.704\,916\,59 \times 10^{21}$	0.991 925 165
KNM4e&5	$3.768\,274\,5 \times 10^{21}$	0.985 607 8	$3.714\,040\,9 \times 10^{21}$	0.9894

Table D.2: Runtime averaged source properties for golden runs used in the corresponding neutrino measurement fit. ρd: column density, ϵ: purity density. Scaling factors are used for scaling of RW fit settings to true physical values (equation 3.10).

From	To	Scale Factor
RW scans after Knm4 (pre-cleaning)	Knm3a	0.3934(55)
6.3 G RW scan after Knm3	Knm3b	0.8880(20)
RW scans after Knm4 (pre-cleaning)	Knm4	0.7815(20)

Table D.3: Factors scaling from the RW activity at the time of RW scans to the effective RW activity value during neutrino mass campaigns Knm3a, Knm3b and Knm4. Values were computed by Max Aker.

E Remaining Single FSDs

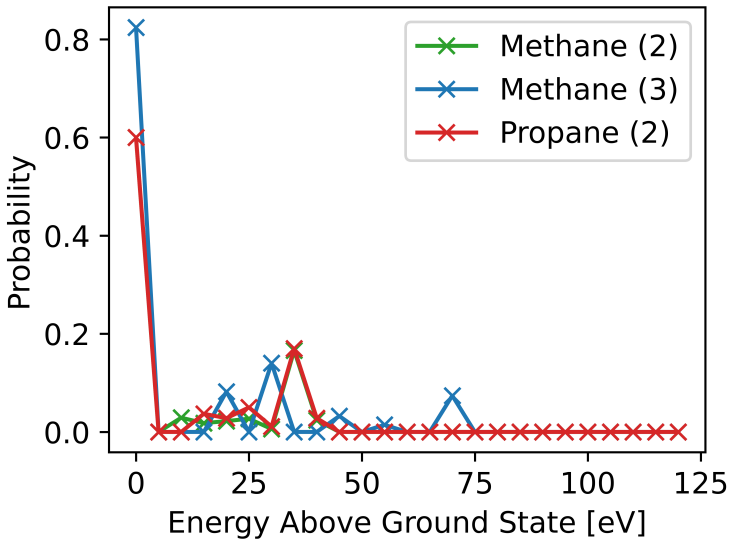

Figure E.1: Single FSDs: Depicted are energies and transition probabilities for methane and propane, but based on different calculations than the ones shown in figures 4.3 and 4.4. Labeled are the parent molecules before the beta decay. States are binned in 5 eV intervals for this plot.
References: methane (2)[29] (3)[30] and propane (2)[30].

F Parametrized FSD Samples

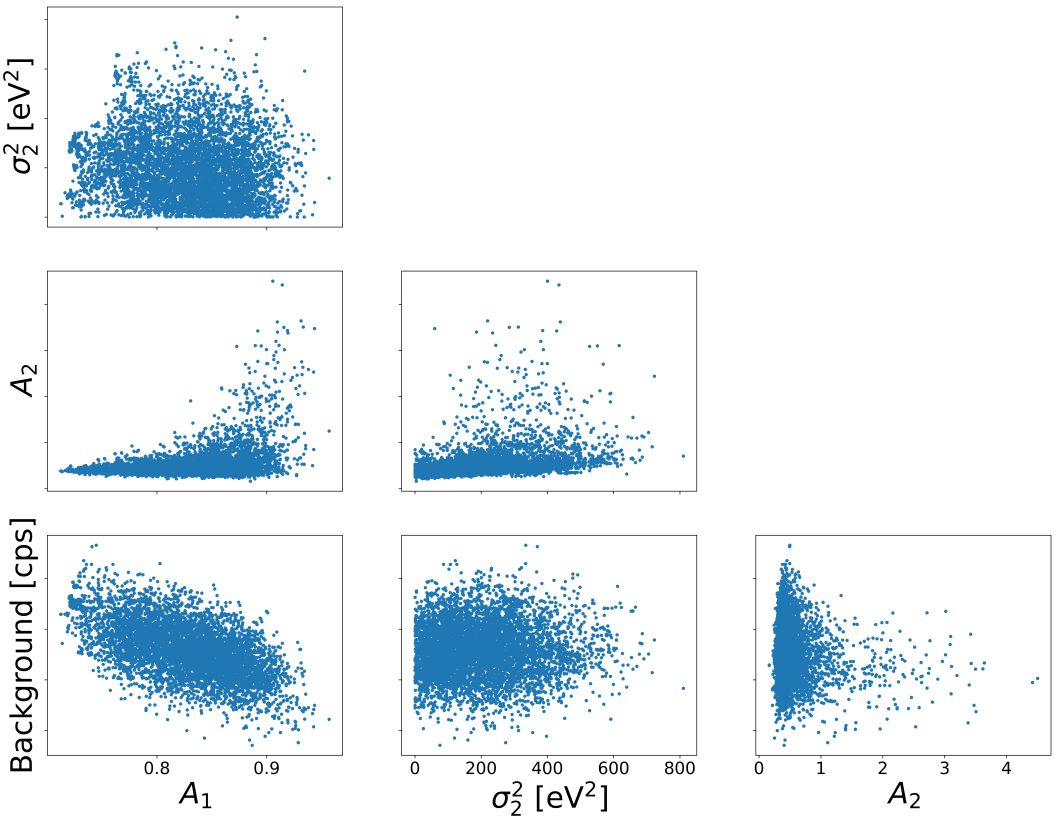

Figure F.1: Parameterized FSD: Pair plot for all samples of the NUTS-MCMC described in section 4.1.5. The first part of this plot is shown in figure F.2.

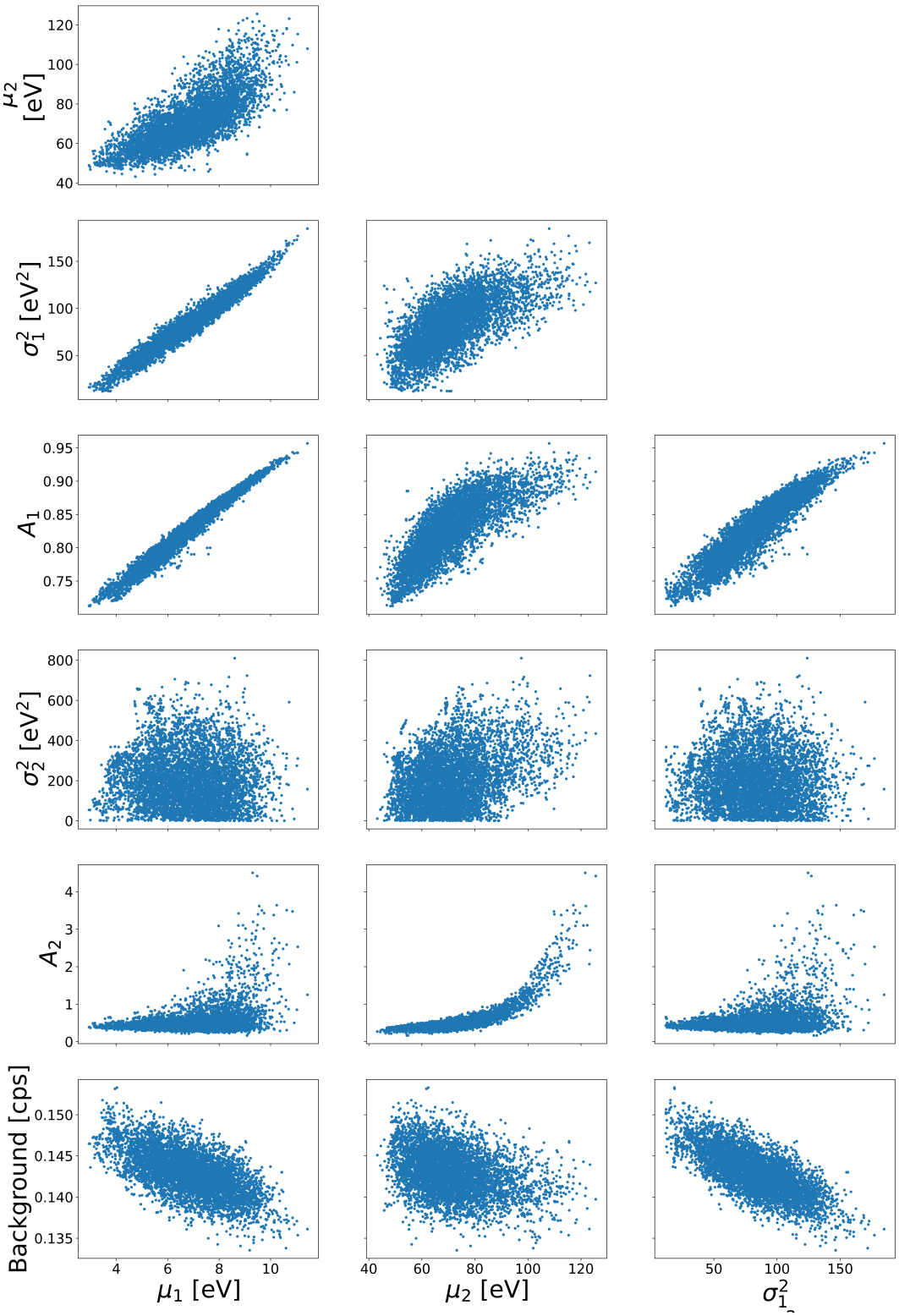

Figure F.2: Parameterized FSD: Pair plot for all samples of the NUTS-MCMC described in section 4.1.5. The second part of this plot is shown in figure F.1.

Bibliography

[1] A. Hermann et al. *Wissenschaftlicher Briefwechsel mit Bohr, Einstein, Heisenberg u.a. Band II: 1930–1939 / Scientific Correspondence with Bohr, Einstein, Heisenberg a.o. Volume II: 1930–1939*. Sources in the History of Mathematics and Physical Sciences. Springer Berlin Heidelberg, 1985. ISBN: 9783662311004.

[2] C. L. Cowan et al. "Detection of the Free Neutrino: a Confirmation." In: *Science* 124.3212 (1956), pp. 103–104. DOI: 10.1126/science.124.3212.103. eprint: https://www.science.org/doi/pdf/10.1126/science.124.3212.103. URL: https://www.science.org/doi/abs/10.1126/science.124.3212.103.

[3] G. Danby et al. "Observation of High-Energy Neutrino Reactions and the Existence of Two Kinds of Neutrinos." In: *Phys. Rev. Lett.* 9 (1 July 1962), pp. 36–44. DOI: 10.1103/PhysRevLett.9.36. URL: https://link.aps.org/doi/10.1103/PhysRevLett.9.36.

[4] K. Kodama et al. "Observation of tau neutrino interactions." In: *Physics Letters B* 504.3 (2001), pp. 218–224. ISSN: 0370-2693. DOI: https://doi.org/10.1016/S0370-2693(01)00307-0. URL: https://www.sciencedirect.com/science/article/pii/S0370269301003070.

[5] Y. Fukuda et al. "Evidence for Oscillation of Atmospheric Neutrinos." In: *Phys. Rev. Lett.* 81 (8 Aug. 1998), pp. 1562–1567. DOI: 10.1103/PhysRevLett.81.1562. URL: https://link.aps.org/doi/10.1103/PhysRevLett.81.1562.

[6] B. Aharmim et al. "Combined analysis of all three phases of solar neutrino data from the Sudbury Neutrino Observatory." In: *Phys. Rev. C* 88 (2 Aug. 2013), p. 025501. DOI: 10.1103/PhysRevC.88.025501. URL: https://link.aps.org/doi/10.1103/PhysRevC.88.025501.

[7] Ziro Maki, Masami Nakagawa, and Shoichi Sakata. "Remarks on the Unified Model of Elementary Particles." In: *Progress of Theoretical Physics* 28.5 (Nov. 1962), pp. 870–880. ISSN: 0033-068X. DOI: 10.1143/PTP.28.870. eprint: https://academic.oup.com/ptp/article-pdf/28/5/870/5258750/28-5-870.pdf. URL: https://doi.org/10.1143/PTP.28.870.

[8] M. Agostini et al. "Final Results of GERDA on the Search for Neutrinoless Double-β Decay." In: *Phys. Rev. Lett.* 125 (25 Dec. 2020), p. 252502. DOI: 10.1103/PhysRevLett.125.252502. URL: https://link.aps.org/doi/10.1103/PhysRevLett.125.252502.

[9] Eleonora Di Valentino, Stefano Gariazzo, and Olga Mena. "Most constraining cosmological neutrino mass bounds." In: *Phys. Rev. D* 104 (8 Oct. 2021), p. 083504. DOI: 10.1103/PhysRevD.104.083504. URL: https://link.aps.org/doi/10.1103/PhysRevD.104.083504.

[10] V. N. Aseev et al. "Upper limit on the electron antineutrino mass from the Troitsk experiment." In: *Phys. Rev. D* 84 (11 Dec. 2011), p. 112003. DOI: 10.1103/PhysRevD.84.112003. URL: https://link.aps.org/doi/10.1103/PhysRevD.84.112003.

[11] Ch Kraus et al. "Final results from phase II of the Mainz neutrino mass searchin tritium β decay." In: *The European Physical Journal C - Particles and Fields* 40.4 (Apr. 2005), pp. 447–468. ISSN: 1434-6052. DOI: 10.1140/epjc/s2005-02139-7. URL: https://doi.org/10.1140/epjc/s2005-02139-7.

[12] M. Aker et al. "First direct neutrino-mass measurement with sub-eV sensitivity." In: (2021). arXiv: 2105.08533 [hep-ex].

[13] KATRIN Collaboration and KATRIN Collaboration. *KATRIN design report 2004*. Tech. rep. 51.54.01; LK 01. Forschungszentrum Jülich, 2005. 245 pp. DOI: 10.5445/IR/270060419.

[14] M. Aker et al. "The design, construction, and commissioning of the KATRIN experiment." In: *Journal of Instrumentation* 16.08 (Aug. 2021), T08015. DOI: 10.1088/1748-0221/16/08/t08015. URL: https://doi.org/10.1088/1748-0221/16/08/t08015.

[15] S. Lukić et al. "Measurement of the gas-flow reduction factor of the KATRIN DPS2-F differential pumping section." In: *Vacuum* 86.8 (2012), pp. 1126–1133. ISSN: 0042-207X. DOI: https://doi.org/10.1016/j.vacuum.2011.10.017. URL: https://www.sciencedirect.com/science/article/pii/S0042207X11003800.

[16] Oliver Rest. "Precision high voltage at the KATRIN experiment and new methods for an absolute calibration at ppm-level for high-voltage dividers." INSTRUMENTATION RELATED TO NUCLEAR SCIENCE AND TECHNOLOGY. PhD thesis. 2019. URL: http://inis.iaea.org/search/search.aspx?orig_q=RN:51004738.

[17] Christian Karl. "Analysis of First Tritium Data of the KATRIN Experiment." Master's Thesis, Technical University of Munich, 2018.

[18] M. Kleesiek et al. "β-Decay spectrum, response function and statistical model for neutrino mass measurements with the KATRIN experiment." In: *The European Physical Journal C* 79.3 (Mar. 2019), p. 204. ISSN: 1434-6052. DOI: 10.1140/epjc/s10052-019-6686-7. URL: https://doi.org/10.1140/epjc/s10052-019-6686-7.

[19] M. Aker et al. "Precision measurement of the electron energy-loss function in tritium and deuterium gas for the KATRIN experiment." In: *The European Physical Journal C* 81.7 (July 2021), p. 579. ISSN: 1434-6052. DOI: 10.1140/epjc/s10052-021-09325-z. URL: https://doi.org/10.1140/epjc/s10052-021-09325-z.

[20] M. Röllig et al. "Activity monitoring of a gaseous tritium source by beta induced X-ray spectrometry." In: *Fusion Engineering and Design* 88.6 (2013). Proceedings of the 27th Symposium On Fusion Technology (SOFT-27); Liège, Belgium, September 24-28, 2012, pp. 1263–1266. ISSN: 0920-3796. DOI: https://doi.org/10.1016/j.fusengdes.2012.11.001. URL: https://www.sciencedirect.com/science/article/pii/S0920379612004632.

[21] Lutz Bornschein et al. "Status of the Karlsruhe Tritium Neutrino Mass Experiment KATRIN." In: *Fusion Science and Technology* 71.4 (2017), pp. 485–490. DOI: 10.1080/15361055.2017.1291241. eprint: https://doi.org/10.1080/15361055.2017.1291241. URL: https://doi.org/10.1080/15361055.2017.1291241.

[22] Laura Kuckert. "The Windowless Gaseous Tritium Source of the KATRIN Experiment - Characterisation of Gas Dynamical and Plasma Properties." 51.03.01; LK 01. PhD thesis. Karlsruher Institut für Technologie (KIT), 2016. 296 pp. DOI: 10.5445/IR/1000065077.

[23] Kerstin Schönung. "Development of a Rear Wall for the KATRIN Rear Section and investigation of tritium compatibility of Rear Section components." PhD thesis. Karlsruher Institut für Technologie (KIT), 2016. 336 pp. DOI: 10.5445/IR/1000056077.

[24] A. Beglarian et al. "Forward Beam Monitor for the KATRIN experiment." In: (2021). arXiv: 2101.11495 [physics.ins-det].

[25] M. Aker et al. "Analysis methods for the first KATRIN neutrino-mass measurement." In: *Phys. Rev. D* 104 (1 July 2021), p. 012005. DOI: 10.1103/PhysRevD.104.012005. URL: https://link.aps.org/doi/10.1103/PhysRevD.104.012005.

[26] Y.-T. Lin et al. "Beta Decay of Molecular Tritium." In: *Phys. Rev. Lett.* 124 (22 June 2020), p. 222502. DOI: 10.1103/PhysRevLett.124.222502. URL: https://link.aps.org/doi/10.1103/PhysRevLett.124.222502.

[27] Karl-Erik Bergkvist. "On Some Atomic Effects in the Tritium β-Spectrum." In: *Physica Scripta* 4.1-2 (July 1971), pp. 23–31. DOI: 10.1088/0031-8949/4/1-2/004. URL: https://doi.org/10.1088/0031-8949/4/1-2/004.

[28] I.G. Kaplan, G.V. Smelov, and V.N. Smutny. "Neutrino rest mass: Account of the electron correlation effect on the restructuring of the electron shell of a molecule in β decay." In: *Physics Letters B* 161.4 (1985), pp. 389–392. ISSN: 0370-2693. DOI: https://doi.org/10.1016/0370-2693(85)90784-1. URL: https://www.sciencedirect.com/science/article/pii/0370269385907841.

[29] T. A. Claxton, S. Schafroth, and P. F. Meier. "Molecular final states after β decay of tritium-substituted molecules." In: *Phys. Rev. A* 45 (9 May 1992), pp. 6209–6216. DOI: 10.1103/PhysRevA.45.6209. URL: https://link.aps.org/doi/10.1103/PhysRevA.45.6209.

[30] I.G. Kaplan and V.N. Smutny. "β-Decay-Induced Rearrangement of the Molecular Electron Shell and the Problem of Determining the Neutrino Rest Mass." In: ed. by Per-Olov Löwdin. Vol. 19. Advances in Quantum Chemistry. Academic Press, 1988, pp. 289–348. DOI: https://doi.org/10.1016/S0065-3276(08)60618-8. URL: https://www.sciencedirect.com/science/article/pii/S0065327608606188.

[31] E. Holzschuh, M. Fritschi, and W. Kündig. "Measurement of the electron neutrino mass from tritium β-decay." In: *Physics Letters B* 287.4 (1992), pp. 381–388. ISSN: 0370-2693. DOI: https://doi.org/10.1016/0370-2693(92)91000-Y. URL: https://www.sciencedirect.com/science/article/pii/037026939291000Y.

[32] Shigeru Ikuta, Suehiro Iwata, and Masashi Imamura. "Ab initio studies of the β^--decay in OHT, NH2T, CH3T, and 14CH4." In: *The Journal of Chemical Physics* 66.10 (1977), pp. 4671–4676. DOI: 10.1063/1.433676. eprint: https://doi.org/10.1063/1.433676. URL: https://doi.org/10.1063/1.433676.

[33] Martin Slezák. *Final state distribution (FSD) onset*. 2018.

[34] Matthew D. Hoffman and Andrew Gelman. "The No-U-Turn Sampler: Adaptively Setting Path Lengths in Hamiltonian Monte Carlo." In: *Journal of Machine Learning Research* 15.47 (2014), pp. 1593–1623. URL: http://jmlr.org/papers/v15/hoffman14a.html.

Acknowledgments

People who I would like to thank for making this thesis possible, as well as writing it enjoyable, include but are not limited to

- **Prof. Dr. Susanne Mertens** for the chance to join the KATRIN collaboration for the course of my thesis

- **Christian Karl** for making every possible effort to advise and support me the entire time

- **The entire group** of fellow students, PhD students and postdocs at the Max Planck Institute for Physics for their kindness and constant support, as well as the organization of encouraging social beer garden events and Weißwurstfrühstücks.